Article

Neuron

Age-Dependent Dopaminergic Neurodegeneration and Impairment of the Autophagy-Lysosomal Pathway in *LRRK*-Deficient Mice

Highlights

- Loss of LRRK causes age-dependent loss of dopaminergic neurons in the SNpc
- Loss of LRRK results in age-dependent increases of apoptosis in the SNpc
- Loss of LRRK leads to age-dependent autophagy impairment in the SNpc
- Loss of LRRK does not cause neurodegeneration in the cerebral cortex and cerebellum

Authors

Emilie Giaime, Youren Tong, Lisa K. Wagner, Yang Yuan, Guodong Huang, Jie Shen

Correspondence

jshen@bwh.harvard.edu

In Brief

Mutations in the *LRRK2* gene are the most common genetic cause of Parkinson's disease. Giaime et al. show an essential role of LRRK in the survival of dopaminergic neurons and the regulation of the autophagy-lysosomal pathway in the aging brain.

Giaime et al., 2017, Neuron *96*, 796–807
November 15, 2017 © 2017 Elsevier Inc.
https://doi.org/10.1016/j.neuron.2017.09.036

CellPress

CellPress

Neuron
Article

Age-Dependent Dopaminergic Neurodegeneration and Impairment of the Autophagy-Lysosomal Pathway in *LRRK*-Deficient Mice

Emilie Giaime,[1] Youren Tong,[1] Lisa K. Wagner,[1] Yang Yuan,[1] Guodong Huang,[1] and Jie Shen[1,2,3,*]
[1]Department of Neurology, Brigham and Women's Hospital
[2]Program in Neuroscience
Harvard Medical School, Boston, MA 02115, USA
[3]Lead Contact
*Correspondence: jshen@bwh.harvard.edu
https://doi.org/10.1016/j.neuron.2017.09.036

SUMMARY

LRRK2 mutations are the most common genetic cause of Parkinson's disease, but LRRK2's normal physiological role in the brain is unclear. Here, we show that inactivation of LRRK2 and its functional homolog LRRK1 results in earlier mortality and age-dependent, selective neurodegeneration. Loss of dopaminergic (DA) neurons in the substantia nigra pars compacta (SNpc) and of noradrenergic neurons in the locus coeruleus is accompanied with increases in apoptosis, whereas the cerebral cortex and cerebellum are unaffected. Furthermore, selective age-dependent neurodegeneration is only present in *LRRK*$^{-/-}$, not *LRRK1*$^{-/-}$ or *LRRK2*$^{-/-}$ brains, and it is accompanied by increases in α-synuclein and impairment of the autophagy-lysosomal pathway. Quantitative electron microscopy (EM) analysis revealed age-dependent increases of autophagic vacuoles in the SNpc of *LRRK*$^{-/-}$ mice before the onset of DA neuron loss. These findings revealed an essential role of LRRK in the survival of DA neurons and in the regulation of the autophagy-lysosomal pathway in the aging brain.

INTRODUCTION

Parkinson's disease (PD) is the most common neurodegenerative movement disorder characterized neuropathologically by the loss of dopaminergic (DA) neurons in the substantia nigra pars compacta (SNpc) and the presence of Lewy bodies (LBs) containing α-synuclein (Spillantini et al., 1997). Mutations in the *leucine-rich repeat kinase 2* (*LRRK2*) gene are the most common genetic cause of PD (Paisán-Ruíz et al., 2004; Shen, 2004; Zimprich et al., 2004), but the underlying pathogenic mechanism and the normal physiological role of LRRK2 are unclear. Previous analysis of *LRRK2*-deficient mice identified no detectable phenotype in the brain but remarkable PD-like changes in the aged kidney, including striking α-synuclein accumulation and aggregation, impairment of protein degradation pathways and increases in apoptosis (Tong et al., 2010, 2012). These unexpected findings in the kidney are consistent with the report that LRRK2 is normally most abundantly expressed in the kidney (Biskup et al., 2007).

The pathogenic mechanism underlying LRRK2 mutations is still hotly debated. On the one hand, the most common LRRK2 mutation G2019S, which resides in the kinase domain and causes PD at relatively low penetrance (Bardien et al., 2010; Hulihan et al., 2008; Kachergus et al., 2005; Lesage et al., 2005; Marder et al., 2015), was reported to increase its autophosphorylation in vitro (Greggio et al., 2006; Nichols et al., 2010; West et al., 2005). These early findings spurred development of LRRK2 kinase inhibitors as therapies for PD (Atashrazm and Dzamko, 2016). On the other hand, overexpression of the G2019S and other mutations in LRRK2 even at very high levels (>10-fold) in transgenic mice generally did not lead to DA neurodegeneration (Li et al., 2009, 2010; Lin et al., 2009; Liu et al., 2015; Melrose et al., 2010; Tsika et al., 2014). Furthermore, other LRRK2 mutations, such as the R1441C/G/H mutations in the GTPase domain and the Y1699C mutation, did not enhance its kinase activity in vitro (Greggio et al., 2006; Nichols et al., 2010; West et al., 2005). Thus, it is critically important to elucidate the normal physiological role of LRRK2 in the brain to shed light on the pathogenic mechanism.

We therefore generated *LRRK*-deficient mice, in which LRRK2 and its functional homolog LRRK1 are inactivated, as LRRK1, which is relatively abundant in the brain (Biskup et al., 2007; Westerlund et al., 2008), may compensate for the loss of LRRK2 in *LRRK2*$^{-/-}$ brains. Unexpectedly, *LRRK1/2* double-knockout (*LRRK* DKO) mice exhibit earlier mortality at ~16 months of age with marked reduction of body weight but largely normal brain weight. Interestingly, *LRRK* DKO mice, but not *LRRK1* or *LRRK2* single-KO mice, develop age-dependent DA neurodegeneration, as shown by age-dependent reduction of DA neurons in the SNpc at 14–15 months but not at younger ages. The cerebral cortex and cerebellum, however, are unaffected, though noradrenergic neurons in the locus coeruleus and medium spiny neurons of the striatum are also reduced in *LRRK* DKO mice at 15 months. The selective, age-dependent neurodegeneration

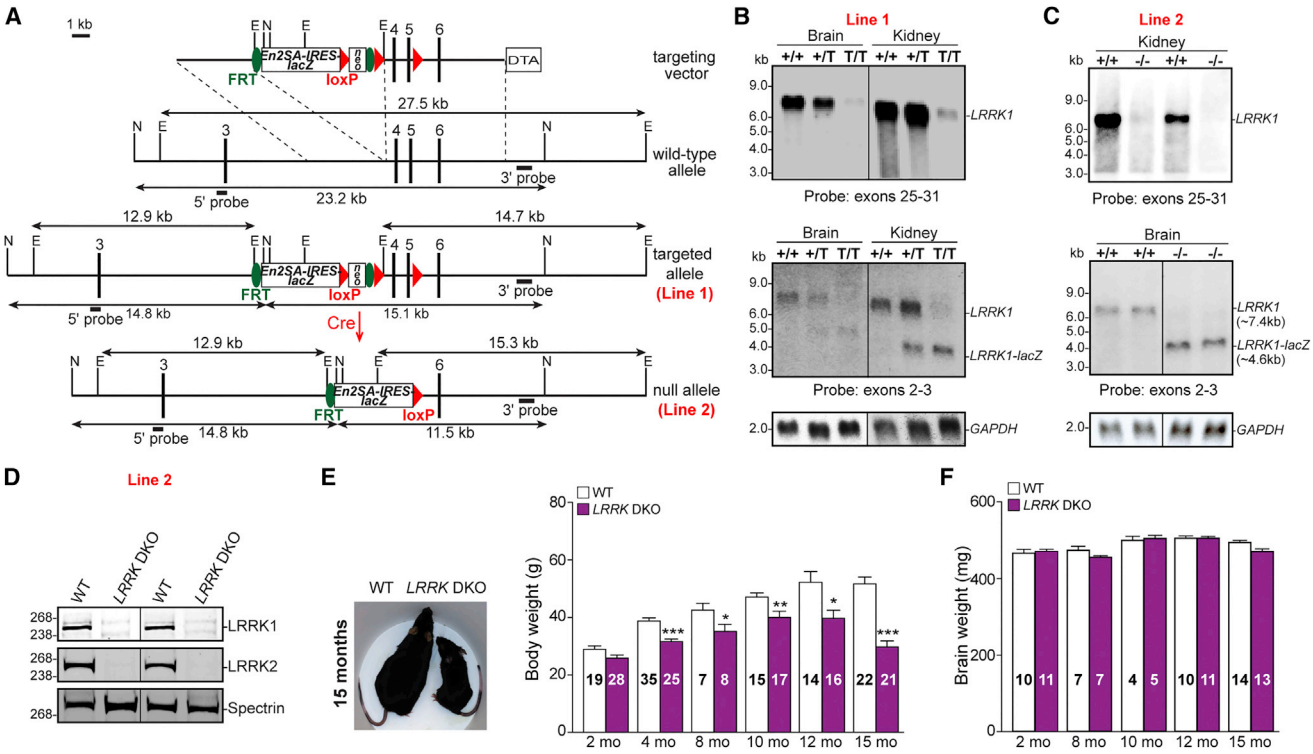

Figure 1. Generation and Molecular Characterization of *LRRK* DKO Mice

(A) Targeting strategy for the generation of *LRRK1* KO mice. The targeting vector contains three *loxP* sites, one in intron 5 and two flanking a *neo* cassette, a gene-trapping sequence (*En2 SA-IRES-lacZ*) flanked by two *FRT* sites in intron 3, which is intended to cause premature termination of *LRRK1* transcription or aberrant RNA splicing. The locations of the 5′ and 3′ external probes for Southern analysis and the expected sizes of the genomic DNA fragments following EcoRV (E) or NheI (N) digestion are shown. The targeted allele resulting from proper homologous recombination events in the 5′ and 3′ arms is designated as Line 1, whereas the *LRRK1*-null allele retains the gene-trapping sequence but lacks exons 4 and 5 following Cre-mediated excision.

(B) Using a downstream cDNA probe specific for *LRRK1* exons 25–31 (1,083 bp), northern analysis of poly(A)+ RNA derived from the brain and kidney of heterozygous and homozygous Line 1 mice carrying the *LRRK1* targeted (T) allele shows the presence of low levels of full-length *LRRK1* mRNA in homozygous T/T mice, indicating that the targeted allele is not a null allele. Using an upstream cDNA probe specific for *LRRK1* exons 2–3 (383 bp), the expected chimeric *LRRK1-lacZ* mRNA is the predominant *LRRK1* transcript, in addition to small amounts of the full-length *LRRK1* mRNA. The vertical lines in the middle of the blot images indicate where superfluous lanes were removed.

(C) Northern analysis of poly(A)+ RNA prepared from the kidney and brain of *LRRK1* KO mice carrying the homozygous *LRRK1*-null allele (Line 2) using the downstream (exons 25–31) and upstream (exons 2–3) probes, respectively, shows the absence of the *LRRK1* full-length mRNA in the kidney and brain of *LRRK1* KO mice and the presence of the chimeric *LRRK1-lacZ* mRNA in *LRRK1* KO brains, which can be revealed by the exons 2–3 probe but not the exons 25–31 probe. The vertical lines in the middle of the blot images indicate where superfluous lanes were removed.

(D) Western analysis of the lung of *LRRK* DKO mice shows the absence of LRRK1 and LRRK2 proteins. The vertical lines in the middle of the blot images indicate where superfluous lanes were removed.

(E) Left: representative image shows *LRRK* DKO and wild-type littermate mice at 15 months of age. Right: bar graphs show reduced weight of *LRRK* DKO mice compared to wild-type mice at 4–15 months of age.

(F) Bar graphs show normal brain weight in *LRRK* DKO mice relative to wild-type controls.

The value in the column indicates the number of mice used in each experiment. All data are expressed as mean ± SEM *p < 0.05, **p < 0.01, ***p < 0.001. See also Figure S1 and Table S1.

is accompanied by increases in apoptotic cell death, increased levels of α-synuclein, and impaired autophagy-lysosomal pathway. Quantitative electron microscopy (EM) analysis further revealed dramatic increases of autophagic vacuoles in the SNpc of *LRRK* DKO mice at 10 months, before the onset of DA neuron loss and increases of apoptosis. These results demonstrate that LRRK is required for age-dependent survival of DA neurons and plays an essential role in the regulation of the autophagy-lysosomal pathway in the aging brain.

RESULTS

Generation and Characterization of *LRRK* DKO Mice

To generate *LRRK*-null mice lacking both LRRK1 and LRRK2, we obtained a targeted *LRRK1* embryonic stem cell (ESC) clone (EPD0073_6_C01) from the KOMP repository (https://www.komp.org/). The targeted *LRRK1* allele contains the gene-trapping *En2SA-IRES-lacZ* and *hbactP-neo* selection cassettes in *LRRK1* intron 3 and a third *loxP* site in intron 5 (Figure 1A). The entire *En2SA-IRES-lacZ* and *hbactP-neo* sequence is flanked

by two *FRT* sites, and the *hbactP-neo* cassette is flanked by two *loxP* sites. The introduction of the gene-trap *En2SA-IRES-lacZ* cassette was intended to cause gene inactivation by premature transcriptional termination, as splicing is expected to occur from the splice donor site of *LRRK1* exon 3 to the splice acceptor site of exon 2 of the *engrailed 2* gene (*En2SA*), leading to the predicted production of a chimeric transcript (*LRRK1-lacZ*) composed of *LRRK1* exons 1–3, *En2* exon 2, *IRES*, and *lacZ* sequences (Figure S1A). We confirmed the ESC clone carrying the targeted allele by Southern blotting using the 5′ and 3′ external probes (Figure S1B) as well as the *neo* probe (data not shown). The chimeric mice resulting from the confirmed ESCs were bred to B6/129 F1 mice to generate targeted *LRRK1* mice, which were termed Line 1 (or "Knockout First" by KOMP). The germline transmission of the targeted *LRRK1* allele was confirmed by Southern blotting using the 5′ and 3′ external probes (data not shown).

Northern analysis of RNA derived from the brain and kidney of mutant mice homozygous for the *LRRK1* targeted allele (Line 1) revealed that there are small amounts of full-length *LRRK1* mRNA using a cDNA probe specific for exons 25–31 (Figure 1B). qRT-PCR using primers specific for exons 30 and 31 confirmed that there are ~19% and ~13% of *LRRK1* mRNA remaining in the brain and the kidney of these mutant mice, respectively (Figure S1C). Using a cDNA probe specific for *LRRK1* exons 2–3, we also detected the anticipated *LRRK1-lacZ* transcript in the brain and kidney of Line 1 targeted *LRRK1* mutant mice (Figure 1B). RT-PCR using primers in exons 3 and 6 followed by sequencing identified not only normal *LRRK1* transcripts (591 bp) retaining all exons examined (exons 3–6) but also an additional aberrant chimeric transcript (706 bp) containing *LRRK1* exon 3, part of *En2* exon 2, and *LRRK1* exons 4–6 (Figure S1D), due to the presence of a putative splice donor site within *En2* exon 2 (Figure S1A). Therefore, the targeted allele (Line 1) is not a null allele as it allows expression of full-length *LRRK1* mRNA as well as aberrant splice products (Figures 1B and S1D).

We then crossed Line 1 with *Cre* deleter mice and removed the floxed *LRRK1* exons 4–5 to generate *LRRK1* deletion mice (Line 2; Figure 1A). Using the external 5′ and 3′ probes, Southern analysis confirmed the deletion of *LRRK1* exons 4–5 in Line 2 mutant mice (Figures S1F and 1A). Northern analysis using cDNA probes specific for exons 25–31 or exons 2–3 revealed no detectable full-length *LRRK1* mRNA in homozygous Line 2 deletion mice (Figure 1C). Extensive RT-PCR analysis followed by sequencing confirmed the absence of full-length *LRRK1* mRNA in these homozygous Line 2 mice (Figure S1G). We therefore concluded that Line 2 represents a null allele and subsequently used this line for all phenotypic analysis. *LRRK* DKO ($LRRK1^{-/-}$; $LRRK2^{-/-}$) mice were obtained at the expected Mendelian ratio from intercrossing $LRRK1^{+/-}$; $LRRK2^{+/-}$ mice (Table S1). Western analysis confirmed the absence of LRRK1 and LRRK2 proteins in the lung of *LRRK* DKO mice, as LRRK1 is most abundant in the lung (Figure 1D).

LRRK DKO mice exhibit striking age-dependent reduction in body weight (Figure 1E), but the brain weight is largely unchanged (Figure 1F). The dramatic weight loss phenotype of *LRRK* DKO mice is absent in *LRRK* mutant mice carrying homozygous Line 1 and *LRRK2*-null alleles (Figure S1E), consistent with the presence of full-length *LRRK1* mRNA in Line 1 mutants (Figures 1B, S1C, and S1D). *LRRK1* KO mice (Line 2) at 15 months also showed reduced body weight but normal brain weight (Figures S1I and S1J), and they did not exhibit earlier mortality. *LRRK* DKO mice die at ~16 months of age with cataracts (Figure S1H).

Age-Dependent Loss of DA Neurons in the SNpc of *LRRK* DKO Mice

To determine whether inactivation of LRRK affects DA neurons in the SNpc, we performed immunostaining in *LRRK* DKO mice using an antibody against tyrosine hydroxylase (TH). The morphology of TH^+ DA neurons in *LRRK* DKO mice at the ages of 2, 8, 12, 14, and 15 months appears normal (Figures 2A and S2F). Stereological neuron counting revealed that the number of TH^+ neurons in the SNpc of *LRRK* DKO mice is significantly reduced (~22%) at 15 months, relative to littermate wild-type controls (Figure 2B), whereas the number of TH^+ neurons in the SNpc of *LRRK1* and *LRRK2* KO mice is unchanged (Figures S2A and S2B). The loss of DA neurons in the SNpc of *LRRK* DKO mice is age dependent, as the number of TH^+ DA neurons in the SNpc of *LRRK* DKO mice is unchanged at the ages of 2 months (Figure 2B), 8 months (Figure S2G), 10 months (data not shown), and 12 months (Figure 2B), but significantly reduced (~16%) at the age of 14 months (Figure 2B). We further performed TH and NeuN double immunostaining of *LRRK* DKO and wild-type mice at 15 months of age and found that the numbers of $NeuN^+$ and $NeuN^+/TH^+$ neurons are also significantly reduced in the SNpc of *LRRK* DKO mice (Figures S2H–S2K).

We also measured the levels of striatal DA and its major metabolites using HPLC. The striatal DA level is significantly reduced in *LRRK* DKO mice at 15 months, compared to their wild-type littermate controls (Figure 2E), whereas DA levels are unchanged in *LRRK* DKO mice at 2 and 8 months (Figure S2D). Levels of dihydroxylphenylacetic acid (DOPAC), one of the major metabolites of DA, are also reduced in the striatum of *LRRK* DKO mice at 15 months (Figure 2F) but not at 2 and 8 months (Figure S2E). These results are consistent with the significant reduction of TH^+ DA neurons in the SNpc of *LRRK* DKO mice at 14–15 months.

Because loss of noradrenergic neurons in the LC has also been reported in PD patients (Forno, 1996), we quantified the number of TH^+ noradrenergic neurons in the LC. The number of noradrenergic neurons in the LC is significantly reduced in *LRRK* DKO mice at 15 months, relative to littermate wild-type controls (Figures 2C and 2D). Thus, LRRK function is required for survival of DA neurons in the SNpc and noradrenergic neurons in the LC.

Age-Dependent, Selective Increases of Apoptosis in the *LRRK* DKO Brain

To determine further whether loss of DA neurons and noradrenergic neurons in *LRRK* DKO mice is due to increases in apoptosis, we used an antibody specific for active caspases-3 and the TUNEL assay to label apoptotic cells. We observed increases of active caspases-3^+ cells in the SNpc and striatum but not in the neocortex in *LRRK* DKO mice at 15 months (Figures 3A and 3B). The number of active caspases-3^+ cells in the

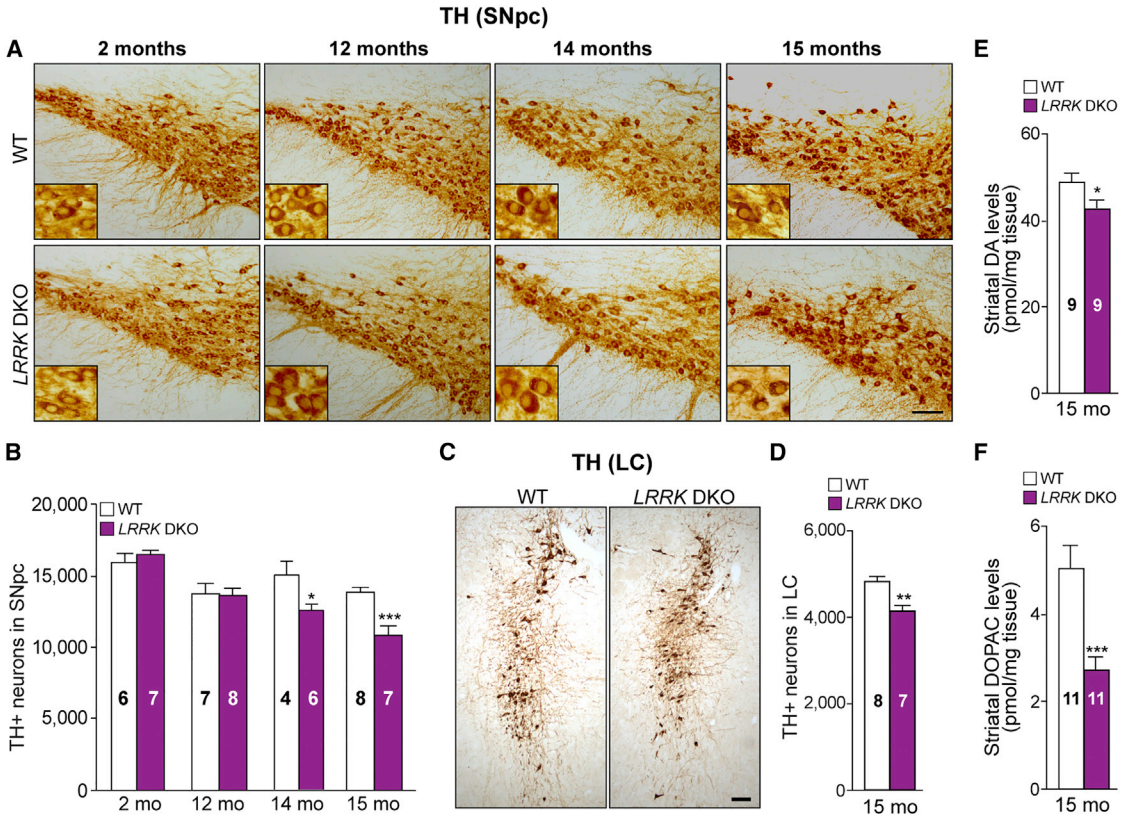

Figure 2. Age-Dependent Loss of DA Neurons in the SNpc of *LRRK* DKO Mice

(A) Immunohistochemical analysis shows similar morphology of TH^+ DA neurons (see higher-power images in the inserts) in the SNpc of *LRRK* DKO and wild-type mice at the ages of 2–15 months.

(B) Stereological neuron count reveals age-dependent reduction (~16% at 14 months, ~22% at 15 months) of DA neurons in the SNpc of *LRRK* DKO mice.

(C) Immunohistochemical analysis shows similar morphology of TH^+ noradrenergic neurons in the LC of *LRRK* DKO and wild-type mice at 15 months.

(D) Stereological neuron count reveals reduction of TH^+ noradrenergic neurons in the LC of *LRRK* DKO mice, relative to littermate wild-type controls.

(E and F) Reduced levels of striatal DA (E) and its metabolite DOPAC (F) measured by HPLC in *LRRK* DKO mice at 15 months, relative to wild-type littermate controls.

The value in the column indicates the number of mice used in each experiment. All data are expressed as mean ± SEM. *$p < 0.05$, **$p < 0.01$, ***$p < 0.001$. Scale bar, 100 μm. See also Figure S2.

SNpc, striatum, and neocortex of *LRRK1* KO and *LRRK2* KO mice at 15 months is much lower than that in *LRRK* DKO mice and is similar to the control (Figures S3A and S3B). Consistent with these findings, the number of $TUNEL^+$ cells is also higher in the SNpc and striatum but not in the neocortex of *LRRK* DKO mice at 15 months of age, relative to control mice (Figures 3C and 3D). At younger ages of 8 months (data not shown) and 12 months (Figures S3C and S3D), we did not observe increases in apoptosis in any of the brain sub-regions of *LRRK* DKO mice, relative to other genotypic groups. The age-dependent and selective increase of apoptotic cell death is consistent with the age-dependent loss of DA neurons in the SNpc of *LRRK* DKO mice.

The increase in apoptosis in the striatum of *LRRK* DKO mice at 15 months prompted us to examine whether the number of medium spiny neurons, which represent >90% of neurons in the striatum and express the highest level of LRRK2 in the brain, is affected in the absence of LRRK. We used DARPP32 immunoreactivity to label medium spiny neurons and found that the number of medium spiny neurons and the volume of the striatum are indeed significantly reduced in *LRRK2* DKO mice at this age (Figures 3E and 3F).

Normal Cerebral Cortex and Cerebellum in *LRRK* DKO Mice

To determine whether loss of LRRK function causes neurodegeneration in other brain sub-regions, we examined the cerebral cortex and the cerebellum. We used stereological methods to quantify the volume and neuron number in the cerebral cortex of *LRRK* DKO mice and wild-type littermate controls at 15 months of age and found that the volume of the cerebral cortex (Figures 4A and 4B) and the number of cortical neurons labeled by NeuN immunoreactivity (Figures 4C and 4D) are unchanged in *LRRK* DKO mice at 15 months. Further quantitative analysis of the cerebellum also showed normal cerebellar volume and number of Purkinje cells labeled by calbindin immunoreactivity in *LRRK* DKO mice at 15 months (Figures 4E–4G). Consistent with selective increases of apoptosis in brain

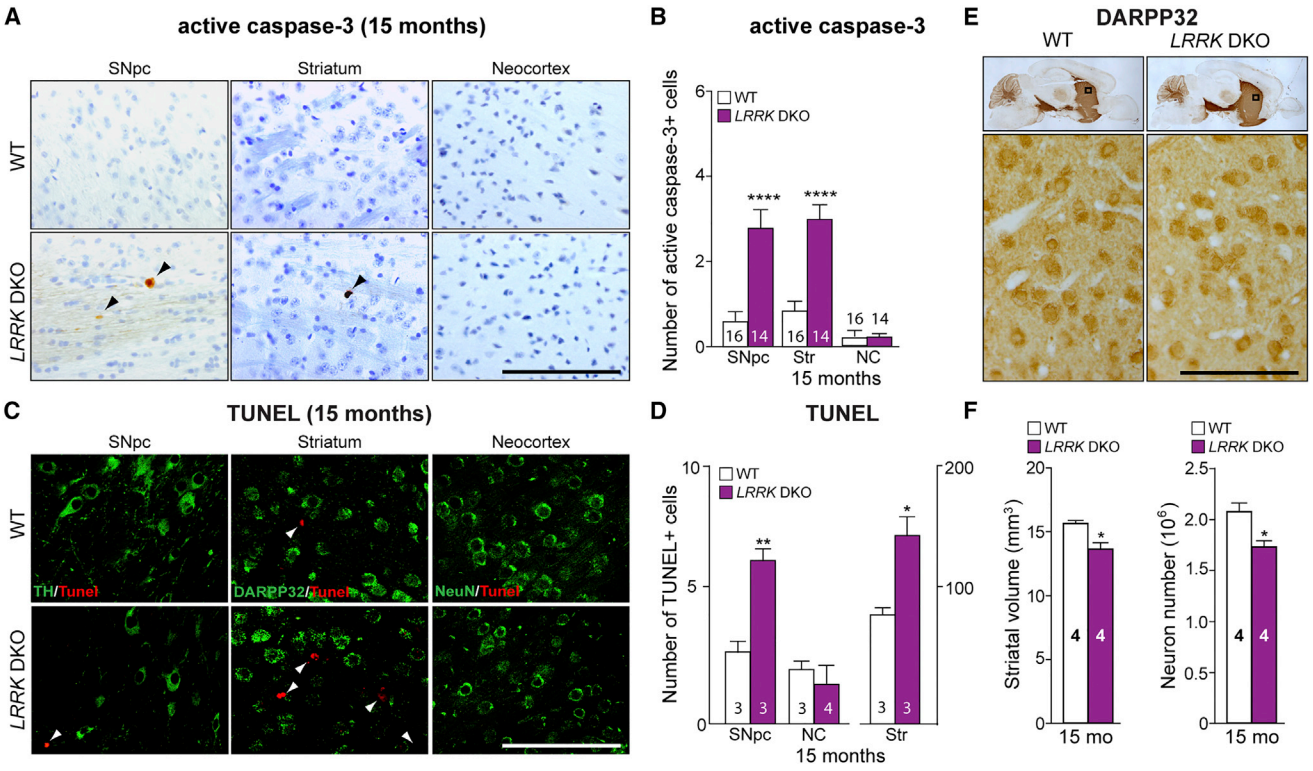

Figure 3. Increases of Apoptotic Cell Death in the *LRRK* DKO Brain at 15 Months of Age

(A) Representative images of active caspases-3 immunoreactivity show apoptotic cells (brown) labeled by black arrowheads in the SNpc, striatum, and neocortex of *LRRK* DKO brains at 15 months of age.

(B) Quantification of active caspase-3$^+$ cells reveals marked increases of apoptotic cells in the SNpc and striatum (Str) but not in the neocortex (NC) of *LRRK* DKO mice, relative to wild-type mice. The average number of apoptotic cells in the SNpc, striatum, or neocortex per brain section is shown, and 3–6 coronal sections per brain (5–10 sections apart) were used for quantification.

(C) Representative images of TH, DARPP-32, or NeuN immunoreactivity (green) and TUNEL (red) show TUNEL$^+$ apoptotic cells labeled by white arrowheads in the SNpc, striatum, and neocortex of *LRRK* DKO brains at 15 months of age.

(D) Quantification of TUNEL$^+$ cells reveals significant increases of apoptotic cells in the SNpc, and striatum but not in the neocortex of *LRRK* DKO mice. The average number of apoptotic cells in the SNpc, striatum, or neocortex per brain section is shown, and coronal sections were used for the SNpc and neocortex and sagittal sections for the striatum.

(E) Top: DARPP-32 immunoreactivity of comparable sagittal sections of *LRRK* DKO and wild-type brains at 15 months of age. Bottom: higher-power views of the boxed areas in the striatum.

(F) Stereological quantification of the striatal volume (left) and DARPP-32$^+$ neurons (right) shows reduced volume and DARPP-32$^+$ medium spiny neurons in the striatum of the *LRRK* DKO brain.

The values in the column indicate the number of mice used in each experiment. All data are expressed as mean ± SEM. *p < 0.05, **p < 0.01, ****p < 0.0001. Scale bars, 100 μm. See also Figure S3.

sub-regions, these results further support the notion that loss of LRRK causes neurodegeneration in a neuron-subtype-specific manner.

Age-Dependent Increases of α-Synuclein in *LRRK* DKO Brains

We previously reported 60-fold increases of α-synuclein monomer in the *LRRK2*$^{-/-}$ kidney at 20 months (Tong et al., 2010), but levels of α-synuclein are unchanged in *LRRK2*$^{-/-}$ kidneys at 15 months (E.G. and J.S., unpublished data). We performed immunohistochemical and western analyses as well as ELISA to evaluate α-synuclein levels in the brain of *LRRK* DKO and control mice. Quantification of α-synuclein immunoreactivity indicated significant increases of α-synuclein in the SNpc and striatum but not in the neocortex of *LRRK* DKO mice at 15 months, relative to littermate wild-type controls (Figures 5A and 5B), though α-synuclein immunoreactivity is unchanged in the SNpc and striatum of *LRRK1* and *LRRK2* single-KO mice (Figures S4A and S4B). Western analysis showed significant increases of α-synuclein monomer and higher-molecular-weight (HMW) species in the striatum of *LRRK* DKO mice (Figures 5C and 5D). ELISA also showed that α-synuclein levels are increased in the striatum but not in the neocortex of *LRRK* DKO mice at 15 months of age (Figure 5E). At 12 and 14 months of age, however, levels of α-synuclein immunoreactivity are not significantly changed in the SNpc, striatum, and neocortex of *LRRK* DKO mice (Figures S4C–S4F). These results indicate that loss of LRRK results in an age-dependent accumulation of α-synuclein in the SNpc and the striatum.

We further examined whether ubiquitin-mediated protein degradation is affected in the brain of *LRRK* DKO mice.

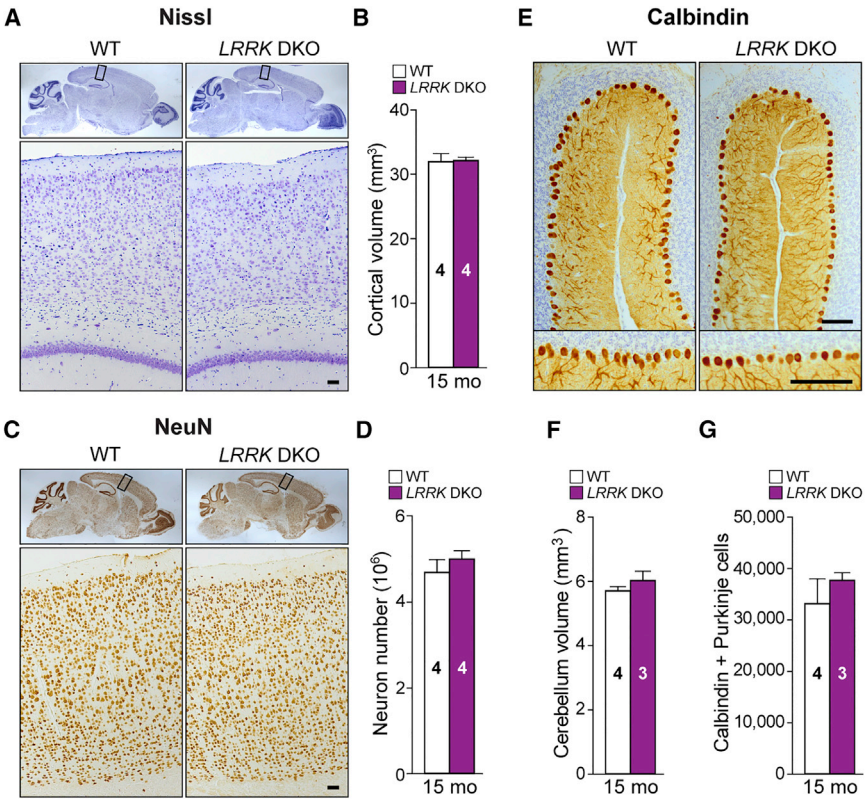

Figure 4. Normal Cerebral Cortex and Cerebellum in *LRRK* DKO Mice

(A) Top: Nissl staining of comparable sagittal sections of *LRRK* DKO and wild-type brains at 15 months of age shows normal gross brain morphology in *LRRK* DKO mice. Bottom: higher-power views of the boxed areas showing no overt alterations in the cerebral cortex.

(B) Stereological quantification shows unchanged volume of the neocortex in *LRRK* DKO mice.

(C) Top: NeuN staining of comparable sagittal sections of *LRRK* DKO and control brains at 15 months of age. Bottom: higher-power views of the boxed areas in the neocortex.

(D) Stereological quantification of the number of $NeuN^+$ neurons in the neocortex shows similar numbers of cortical neurons in *LRRK* DKO and control brains at 15 months.

(E) Top: immunohistochemical analysis of comparable sagittal sections stained with a calbindin antibody shows normal morphology of Purkinje cells in the cerebellum of *LRRK* DKO mice at 15 months of age. Bottom: higher-power views of the Purkinje cell layer in the cerebellum.

(F and G) Stereological quantification shows unchanged cerebellar volume (F) and number of $calbindin^+$ Purkinje cells (G) in *LRRK* DKO brains at 15 months.

The values in the column indicate the number of mice used in each experiment. All data are expressed as mean ± SEM. Scale bar, 100 μm.

Immunohistochemical analysis revealed significant increases of ubiquitin immunoreactivity in the striatum of *LRRK* DKO mice at 15 months (Figures S4G and S4H). Consistent with this finding, western analysis showed significant increases of HMW species immunoreactive for ubiquitin-specific antibodies in the striatum of *LRRK* DKO mice at 15 months (Figures S4I and S4J) but not at 12 months (data not shown), suggesting an age-dependent accumulation of ubiquitinated proteins in the absence of LRRK.

Age-Dependent Autophagy Impairment in *LRRK* DKO Brains

To determine whether the autophagy-lysosomal pathway is affected in *LRRK* DKO brains during aging we evaluated p62, an autophagy substrate that binds to ubiquitin and forms complexes with LC3 (Bjørkøy et al., 2005; Ichimura et al., 2008). We found significant increases of p62 immunoreactivity in different brain sub-regions, including the SNpc, striatum, neocortex, and optic tract in *LRRK* DKO mice at 15 months (Figures 6A and 6B). Western analysis also showed significant increases of p62 in the dissected striatum, neocortex, and optic nerve of *LRRK* DKO mice at 15 months (Figures 6C–6E). We did not detect significant alterations in p62 immunoreactivity in the SNpc and striatum of *LRRK1* and *LRRK2* single-KO at 15 months of age (Figures S5A and S5B). Immunohistochemical analysis also showed co-localization of p62 and ubiquitin immunoreactivity in the optic tract of *LRRK* DKO mice at 15 months (Figure 6G). We further examined conversion of LC3-I, a homolog of Atg8 (Kabeya et al., 2000; Kirisako et al., 1999), to the lipidated form, LC3-II, which is essential for the formation of autophagosomes and is a marker of autophagosome formation and accumulation (Mizushima et al., 2010). We observed significant decreases of LC3-I levels and increases of LC3-II levels in the optic tract of *LRRK* DKO mice at 15 months (Figures 6E and 6F), further indicating autophagy impairment.

Age-Dependent Increases of Autophagic Vacuoles in the SNpc of *LRRK* DKO Mice

We further performed transmission EM analysis of *LRRK* DKO and wild-type neurons in the SNpc at the ages of 3, 10, and 15 months and found age-dependent accumulation of electron-dense autophagic vacuoles in *LRRK* DKO neurons (Figure 7). At 3 months, there are very few electron-dense vacuoles and the number is not significantly different between *LRRK* DKO and wild-type neurons in the SNpc (Figures 7A, 7D, and 7K). At 10 months, more electron-dense vacuoles were found in *LRRK* DKO neurons relative to controls (Figures 7B, 7E, and 7K). At 15 months of age, the number of electron-dense vacuoles is further increased in *LRRK* DKO neurons compared to wild-type neurons (Figures 7C,7F, and 7K). Higher-magnification views further revealed the presence of both autophagosome and autolysosome vacuoles in *LRRK* DKO neurons at 10 and 15 months of age (Figures 7G–7J). We also observed large electron-dense lipofuscin granules composed of lipid components defined as largely round lipid vacuoles (Figures 7G–7J). These ultrastructural changes are consistent with age-dependent impairment of autophagic activity (Figure 6), demonstrating that loss of *LRRK* results in accumulation of autophagic vacuoles and

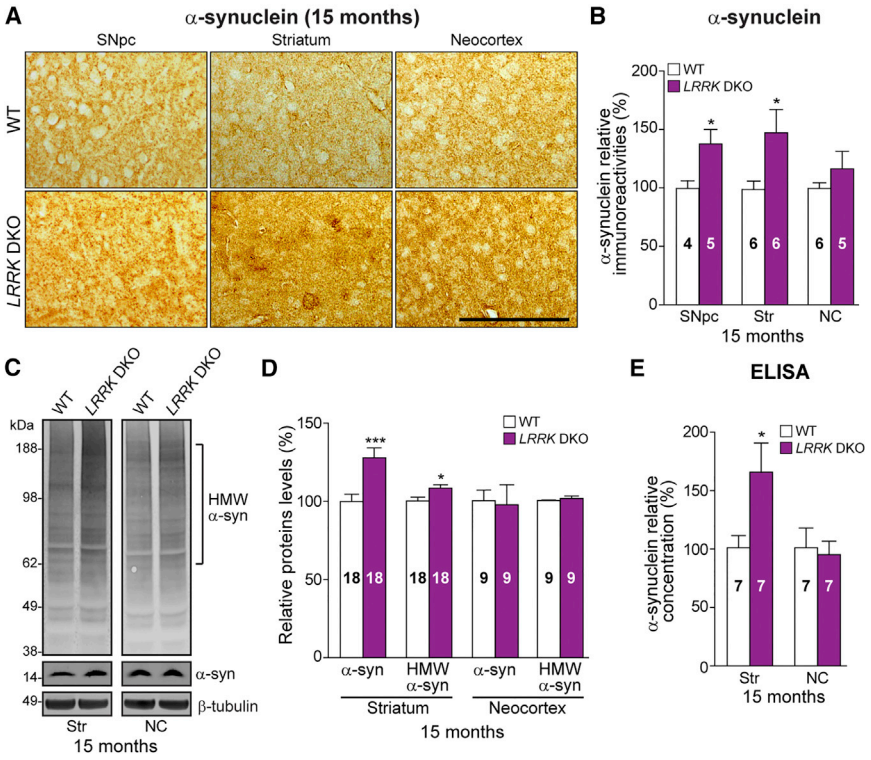

Figure 5. Accumulation of α-Synuclein in the *LRRK* DKO Brain at 15 Months of Age

(A) α-synuclein immunoreactivity in the SNpc, striatum, and neocortex of *LRRK* DKO and littermate control mice at 15 months of age.

(B) Quantification of α-synuclein immunoreactivity reveals significant increases of α-synuclein in the SNpc and striatum but not the neocortex of *LRRK* DKO mice, relative to littermate controls.

(C) Western analysis of α-synuclein in the Triton X-100 soluble fraction of the striatum and neocortex of *LRRK* DKO and wild-type mice at 15 months.

(D) Quantification of α-synuclein monomer and high-molecular weight (HMW) species shows significant increases of α-synuclein monomer and HMW species in the striatum of *LRRK* DKO mice, relative to wild-type controls.

(E) ELISA shows significant increases of α-synuclein levels in the striatum of *LRRK* DKO mice, relative to wild-type controls.

The value in the column indicates the number of mice used in each experiment. All data are expressed as mean ± SEM. *p < 0.05, **p < 0.01, ***p < 0.001. Scale bars, 100 μm. See also Figure S4.

lipofuscin granules, leading to impaired protein/lipid degradation and autophagy function in aging neurons in the SNpc.

DISCUSSION

Mutations in LRRK2 are collectively the most common genetic cause of PD, associated with both familial and sporadic cases (Nalls et al., 2014; Paisán-Ruíz et al., 2004; Satake et al., 2009; Simón-Sánchez et al., 2009; Zimprich et al., 2004), highlighting the importance of LRRK2 in PD pathogenesis (Cookson, 2015; Pan and Yue, 2014; Tsika and Moore, 2012). Genetic analysis revealed striking age-dependent autophagy impairment and accumulation of α-synuclein as well as increases of apoptosis in the *LRRK2*$^{-/-}$ kidney (Tong et al., 2010, 2012). However, there is no loss of DA neurons reported in the *LRRK2*$^{-/-}$ brain (Hinkle et al., 2012; Tong et al., 2010), raising the possibility that LRRK1 may compensate for the loss of LRRK2 in the brain. Indeed, complete inactivation of LRRK1 and LRRK2 results in age-dependent loss of DA neurons in the SNpc and noradrenergic neurons in the LC as well as reduced levels of striatal DA and its metabolites (Figures 1 and 2). Furthermore, age-dependent neurodegeneration is selective in the SNpc, LC and striatum of *LRRK* DKO mice, whereas the cerebral cortex and cerebellum are unaffected (Figure 4). The selective neuronal loss in the SNpc and striatum is accompanied by increases of apoptosis (Figure 3), enhanced α-synuclein levels (Figure 5), and impaired autophagy (Figure 6). Quantitative EM analysis further showed age-dependent accumulation of autophagic vacuoles in the SNpc of *LRRK* DKO mice (Figure 7), before the onset of DA neuron loss and increases in apoptosis in the SNpc. Together, these findings demonstrate that LRRK plays a critical role in the regulation of the autophagy-lysosomal pathway and survival of DA neurons in the aging brain.

Essential Role of LRRK in DA Neuronal Survival

The motor symptoms associated with PD are caused by loss of DA neurons in the SNpc. Our genetic analysis revealed an essential role of LRRK in support of DA neuron survival during aging, as indicated by the normal number of DA neurons in the SNpc of *LRRK* DKO mice at 2, 8, 10, and 12 months of age, and age-dependent, progressive reduction of DA neurons at 14 and 15 months (Figures 2 and S2). The loss of DA neurons is associated with age-dependent increases of apoptotic cell death in the SNpc of *LRRK* DKO mice, as shown by significant increases of active caspase-3$^+$ and TUNEL$^+$ cells in the SNpc of *LRRK* DKO mice at 15 months but not at 12 months (Figures 3 and S3). Age-dependent neurodegeneration is selective, as the cerebral cortex and the cerebellum of *LRRK* DKO mice at 15 months are not affected (Figure 4), but neurodegeneration is not restricted to DA neurons. We also observed significant reduction of noradrenergic neurons in the LC of *LRRK* DKO mice at 15 months (Figure 2), which are also vulnerable in PD, and increases of caspase-3$^+$ apoptotic cells (data not shown). Furthermore, the volume of the striatum and the number of medium spiny neurons, which represent >90% of neurons in the striatum and express highest levels of LRRK2 in the brain, are also reduced in *LRRK* DKO mice at 15 months, accompanied with significant increases of apoptotic cells in the striatum (Figures 3 and S3). Thus, DA neurons in the SNpc, along with noradrenergic neurons in the LC and GABAergic medium spiny

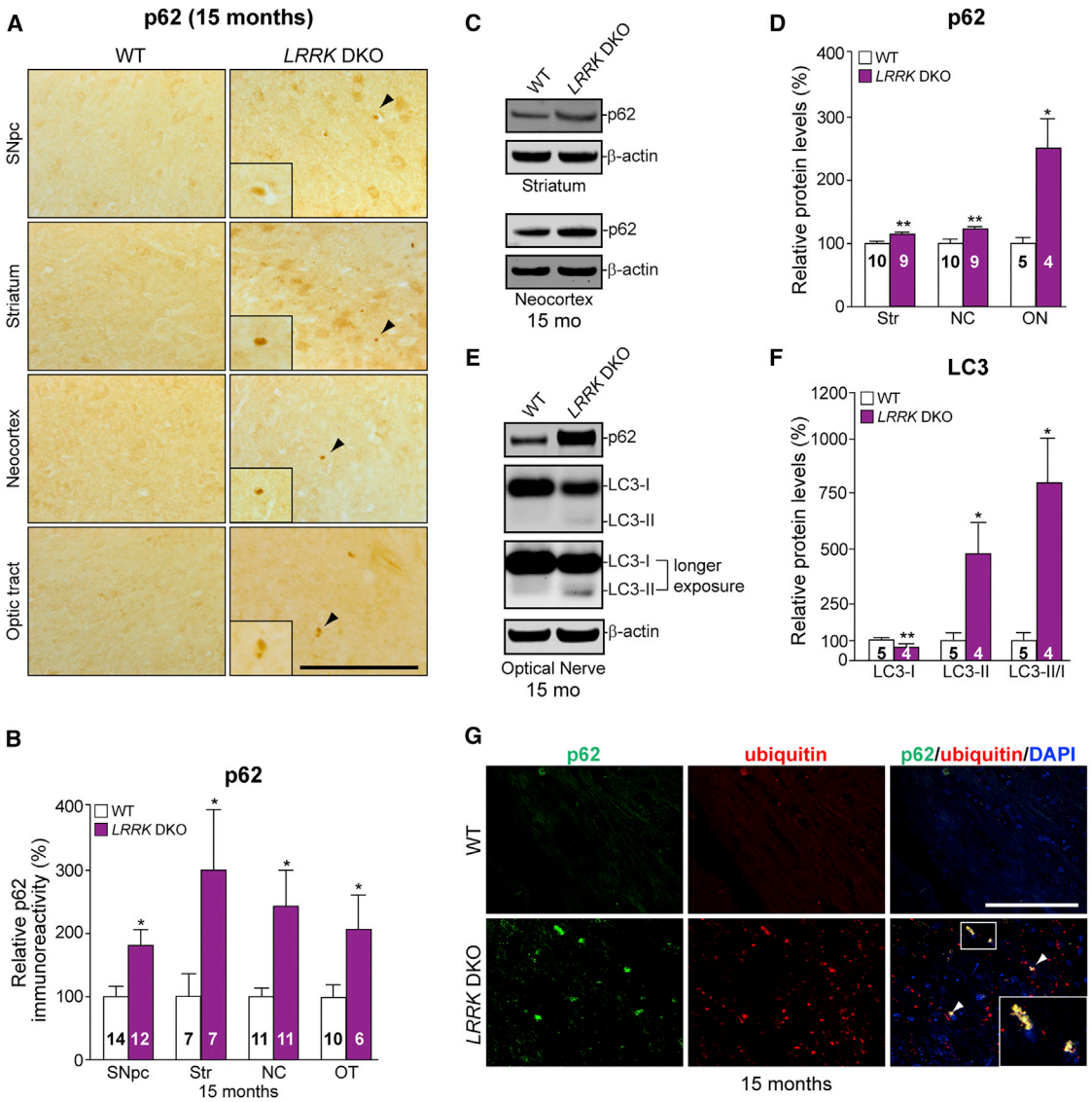

Figure 6. Autophagy Impairment in the *LRRK* DKO Brain at 15 Months of Age

(A) Representative images of immunochemical analysis shows the presence of p62-immunoreactive aggregates marked by black arrowheads (higher-power views in the inserts) in the SNpc, striatum, neocortex, and optic tract of *LRRK* DKO mice at 15 months of age.

(B) Quantification of p62 immunoreactivity in the SNpc, Str, NC, and optic tract (OT) of *LRRK* DKO and wild-type mice reveals marked increases of p62 immunoreactivity in *LRRK* DKO mice.

(C) Western analysis of p62 in Triton X-100-soluble fractions of the dissected striatum and neocortex of *LRRK* DKO and control mice at 15 months.

(D) Quantification of p62 shows significant increases of p62 levels in the striatum, neocortex, and optical nerve (ON) of *LRRK* DKO mice, relative to wild-type controls.

(E) Western analysis of p62, LC3-I, and LC3-II in Triton X-100-soluble fractions of the dissected optical nerve of *LRRK* DKO and wild-type mice at 15 months. A longer exposure is used to reveal LC3-II signals.

(F) Quantification of LC3-I and LC3-II levels shows decreases of LC3-I levels and increases of LC3-II levels in the optical nerve of *LRRK* DKO mice.

(G) Confocal microscopic images show the co-localization of $p62^{+}$ and $ubiquitin^{+}$ aggregates (white arrowheads) in the optical tract of *LRRK* DKO brains at 15 months of age.

The values in the column indicate the number of mice used in each experiment. All data are expressed as mean ± SEM. *$p < 0.05$, **$p < 0.01$. Scale bars, 100 μm. See also Figure S5.

neurons in the striatum, are more vulnerable to the loss of LRRK function during aging.

The lethality of *LRRK* DKO mice at ~16 months of age precluded further examination of older mice to determine the full impact of aging on the brain in the absence of LRRK. The cause of the earlier lethality in *LRRK* DKO mice is unclear, though metabolic analysis of these mice showed age-dependent decreases of food intake and fat content (E.G., L.K.W., and J.S.,

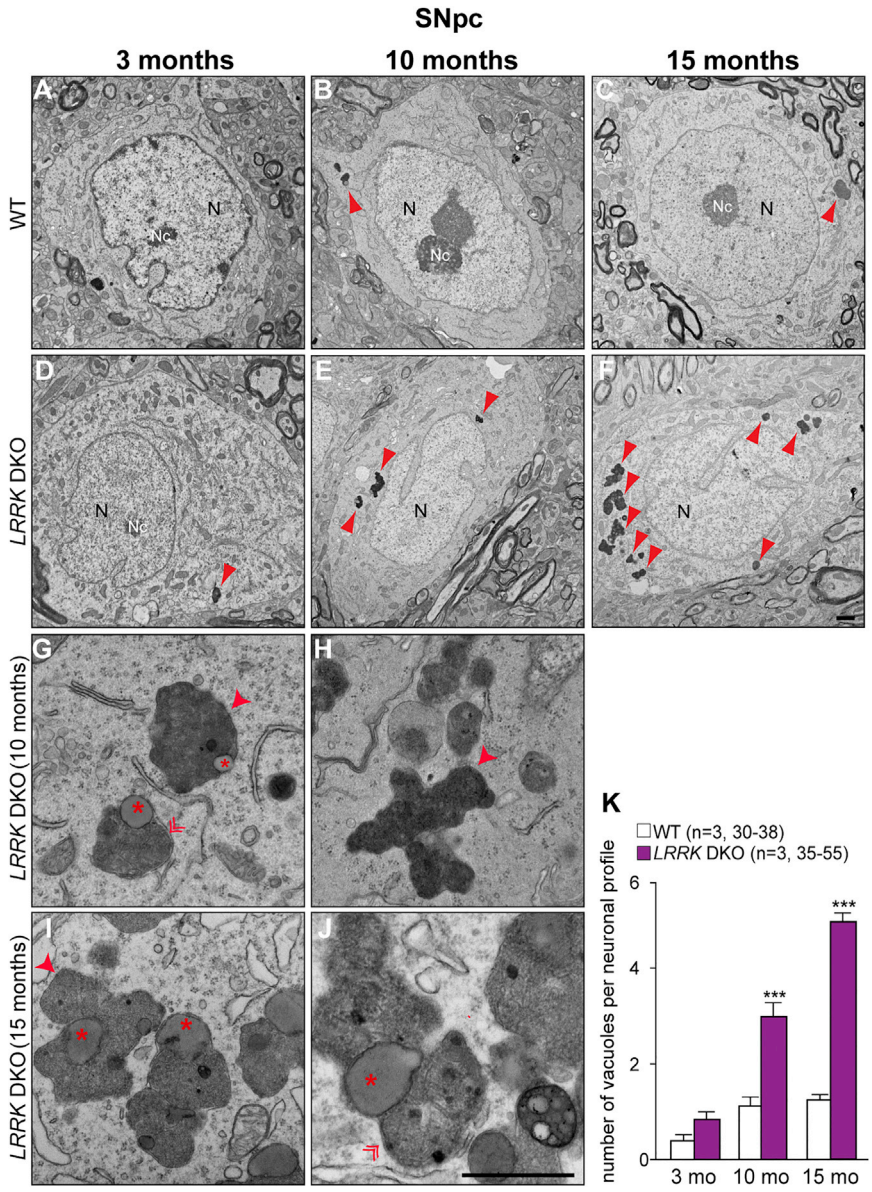

Figure 7. Age-Dependent Increases of Electron-Dense Vacuoles in the SNpc of *LRRK* DKO Mice

(A–C) Representative EM images show electron-dense vacuoles (arrowheads) in the SNpc of wild-type mice at the age of 3 months (A), 10 months (B), and 15 months (C).

(D–F) Representative EM images show increased numbers of electron-dense vacuoles (arrowheads) in the SNpc of *LRRK* DKO brains at the ages of 3 months (D), 10 months (E), and 15 months (F).

(G–J) Higher-power views show various electron-dense autophagic vacuoles containing autolysosomes (single arrowheads), autophagosomes (double arrowheads), or lipofuscin inclusions (asterisks) in the SNpc of *LRRK* DKO mice at 10 months (G and H) and 15 months (I and J).

(K) Quantification of electron-dense vacuoles greater than 0.5 μm in diameter per neuronal profile reveals age-dependent increases in the SNpc of *LRRK* DKO mice.

The values in parentheses indicate the number of mice (left) and neurons (right) used in each experiment. All data are expressed as mean ± SEM ***$p < 0.001$. Scale bars, 500 nm.

unpublished data). While *LRRK* DKO mice show marked age-dependent reduction of body weight, their brain weight is largely unaffected (Figure 1). Furthermore, the body weight is similarly reduced in *LRRK1* KO and *LRRK* DKO mice at 15 months (Figure S1), but the loss of DA neurons in the SNpc is only present in *LRRK* DKO mice but not in *LRRK1* KO or *LRRK2* KO mice (Figure S2). Therefore, selective, age-dependent neurodegeneration in *LRRK* DKO mice is unlikely caused by the gross abnormalities observed in these mice. However, development of DA neuron-specific *LRRK* conditional KO mice will address this question unequivocally and will determine the full extent of aging and loss of LRRK function in DA neuron survival. Furthermore, selective inactivation of LRRK in GABAergic medium spiny neurons in the striatum will determine whether loss of these neurons in *LRRK* DKO mice is cell autonomous.

Regulation of the Autophagy-Lysosomal Pathway by LRRK

The mechanism underlying selective, age-dependent neurodegeneration and accompanying increases of apoptosis in *LRRK* DKO brains is not yet clear. Inhibition of autophagy has previously been reported to induce apoptotic neuronal death (Hara et al., 2006; Komatsu et al., 2006), and conditional inactivation of Atg7 results in age-dependent neurodegeneration (Komatsu et al., 2007). Interestingly, we observed significant increases of the autophagy substrate p62 in the SNpc of *LRRK* DKO brains at 15 months but not at 12 months (Figures 6 and S5), suggesting that the autophagy impairment may underlie the apoptotic cell death in the SNpc of *LRRK* DKO brains. Furthermore, quantitative EM analysis showed that the number of electron dense autophagic vacuoles is markedly increased in the SNpc of *LRRK* DKO mice at 10 months and further increased at 15 months (Figure 7). The age-dependent accumulation of autophagic vacuoles in the SNpc of *LRRK* DKO mice is consistent with defects in autophagic flux reported in *LRRK1*$^{-/-}$ mouse embryonic fibroblasts (Toyofuku et al., 2015). The detailed mechanism by which LRRK regulates the autophagy-lysosomal pathway, however, is not yet clear and awaits further investigation. While the age-dependent autophagy impairment and DA neurodegeneration observed in *LRRK* DKO brains are correlative not causative, the fact that the accumulation of autophagic vacuoles precedes the onset of DA neurodegeneration in *LRRK* DKO brains suggests that the autophagy impairment may contribute

to the increase in apoptosis and neurodegeneration in *LRRK* DKO brains.

Similarly, as we observed in *LRRK2*$^{-/-}$ kidneys (Tong et al., 2010, 2012), levels of α-synuclein are higher in the SNpc and striatum of *LRRK* DKO mice at 15 months of age (Figure 5), further confirming the close link between LRRK2 and α-synuclein, which was reported by other groups as well (Lin et al., 2009; Skibinski et al., 2014). However, while α-synuclein accumulation is striking in *LRRK2*$^{-/-}$ kidneys at 20 months (Tong et al., 2010), increases of α-synuclein levels are much smaller in the SNpc and striatum of *LRRK* DKO brains. This is likely due to the age dependency of α-synuclein accumulation and the earlier lethality of *LRRK* DKO mice, which precludes analysis of these mice at older ages. For example, levels of α-synuclein are normal in *LRRK2*$^{-/-}$ kidneys at 15 months (E.G. and J.S. unpublished data) but are ~60-fold higher than control mice at 20 months, highlighting the effect of aging on α-synuclein accumulation in the absence of LRRK2. The findings that significant increases of α-synuclein in *LRRK* DKO brains were only observed at 15 months but not at 12 or 14 months (Figures 5 and S4), when autophagy impairment was already present, suggest that α-synuclein accumulation is the consequence of autophagy impairment. However, overexpression of α-synuclein in transgenic mice results in age-dependent neurodegeneration (Chandra et al., 2005; Giasson et al., 2002; Lee et al., 2002; Lin et al., 2009). It is therefore possible that α-synuclein accumulation may further contribute to neuronal death during aging. It will be interesting to determine the full impact of aging on α-synuclein accumulation in DA neurons of *LRRK* conditional KO mice and whether introduction of *α-synuclein* transgenes will further exacerbate DA neurodegeneration in these mice.

Molecular Mechanisms Underlying LRRK Function

Despite our findings demonstrating the regulatory role of LRRK in autophagy and neuronal survival in vivo, the underlying molecular mechanism is unclear. Because LRRK2 contains a kinase domain, major efforts have been focused on the identification of its kinase substrates. Using two independent phosphoproteomic screens, Rab10 (pT73) and LRRK2 (pS935) were identified recently as substrates of LRRK2′s kinase activity, and subsequent analysis yielded Rab8a (pT72), Rab3a (pT86), and Rab12 (pS106) as additional substrates (Steger et al., 2016). Furthermore, autophosphorylation of LRRK2 at Ser1292 has also been reported (Sheng et al., 2012). The lack of phospho-specific antibodies, however, makes it difficult to evaluate whether the phospho-protein levels are altered in the absence of LRRK. While the physiological significance of these phosphorylation events and how these Rab proteins may be involved in mediating LRRK2 physiological function are unclear, several genome-wide association studies (GWAS) revealed that the PARK16 locus, which contains 5 transcription units including *RAB7L1*, is associated with sporadic PD (Satake et al., 2009; Simón-Sánchez et al., 2009; Tucci et al., 2010). These association studies suggest that LRRK2 and Rab GTPases may interact in the pathogenesis of PD. Interestingly, *Rab7L1*-deficient mice share similar kidney phenotypes and lysosomal defects as *LRRK2*$^{-/-}$ mice, providing further support for a functional connection between LRRK2 and Rab proteins (Kuwahara et al., 2016). Future studies will be needed to elucidate how LRRK2 interacts with RAB7L1 and other Rab proteins in the regulation of the autophagy-lysosomal pathways. It will also be interesting to determine whether kinase activity is essential for the LRRK-mediated in vivo functions.

In summary, our current study revealed the essential role of LRRK in the regulation of the autophagy-lysosomal pathway and survival of selective neuronal populations in the aging brain. Loss of LRRK function in the mouse brain recapitulates several key features of PD, including age-dependent loss of DA neurons in the SNpc and noradrenergic neurons in the LC, impairment of the protein degradation pathways, α-synuclein accumulation, and increases of apoptosis. The earlier lethality of *LRRK* DKO mice, however, precluded further analysis of older mice to reveal the full impact of aging on DA neuron survival in the absence of LRRK. Conditional KO mice restricting LRRK inactivation to DA neurons only would be necessary to uncover the cell-autonomous consequences of loss of LRRK function on DA neurons, and future studies will be needed to elucidate the molecular mechanism by which LRRK regulates the autophagy-lysosomal pathway and protects DA neurons during aging.

STAR★METHODS

Detailed methods are provided in the online version of this paper and include the following:

- KEY RESOURCES TABLE
- CONTACT FOR REAGENT AND RESOURCE SHARING
- EXPERIMENTAL MODEL AND SUBJECT DETAILS
  - Mouse Strains and Animal Care
- METHOD DETAILS
  - Generation of *LRRK1*$^{-/-}$ and *LRRK*$^{-/-}$ mice
  - Northern analysis
  - RT-PCR
  - Western analysis
  - Histological analysis
  - Immunohistochemical analysis
  - Stereological neuron count
  - TUNEL
  - Measurements of striatal DA and its metabolites by HPLC
  - ELISA
  - Quantitative EM analysis
- QUANTIFICATION AND STATISTICAL ANALYSIS

SUPPLEMENTAL INFORMATION

Supplemental Information includes five figures and one table and can be found with this article online at https://doi.org/10.1016/j.neuron.2017.09.036.

AUTHOR CONTRIBUTIONS

J.S. conceived and directed the project, Y.T. generated the mice, performed the molecular characterization, and made the initial discovery of DA neurodegeneration in *LRRK* DKO mice, E.G. performed most of the phenotypic characterization, L.K.W. performed the quantitative EM analysis, Y.Y. and G.H. performed some phenotypic analysis and validated the data, and J.S., Y.T., E.G., and L.K.W. wrote the paper.

ACKNOWLEDGMENTS

We thank Michael Frotscher for advice on the quantitative EM study, Huailong Zhao for technical assistance, and the Shen lab members for discussion. We also thank the KOMP Repository (https://www.komp.org/) funded by the trans-NIH Knock-Out Mouse Project for the ESC clone used in the generation of *LRRK1* KO mice. This work was supported by grants from the NINDS (R01NS071251 and P50NS094733 to J.S.).

Received: August 10, 2017
Revised: September 14, 2017
Accepted: September 22, 2017
Published: October 19, 2017

REFERENCES

Atashrazm, F., and Dzamko, N. (2016). LRRK2 inhibitors and their potential in the treatment of Parkinson's disease: Current perspectives. Clin. Pharmacol. *8*, 177–189.

Bardien, S., Marsberg, A., Keyser, R., Lombard, D., Lesage, S., Brice, A., and Carr, J. (2010). LRRK2 G2019S mutation: Frequency and haplotype data in South African Parkinson's disease patients. J Neural Transm (Vienna) *117*, 847–853.

Biskup, S., Moore, D.J., Rea, A., Lorenz-Deperieux, B., Coombes, C.E., Dawson, V.L., Dawson, T.M., and West, A.B. (2007). Dynamic and redundant regulation of LRRK2 and LRRK1 expression. BMC Neurosci. *8*, 102.

Bjørkøy, G., Lamark, T., Brech, A., Outzen, H., Perander, M., Øvervatn, A., Stenmark, H., and Johansen, T. (2005). p62/SQSTM1 forms protein aggregates degraded by autophagy and has a protective effect on huntingtin-induced cell death. J. Cell Biol. *171*, 603–614.

Chandra, S., Gallardo, G., Fernández-Chacón, R., Schlüter, O.M., and Südhof, T.C. (2005). Alpha-synuclein cooperates with CSPalpha in preventing neurodegeneration. Cell *123*, 383–396.

Cookson, M.R. (2015). LRRK2 pathways leading to neurodegeneration. Curr. Neurol. Neurosci. Rep. *15*, 42.

Forno, L.S. (1996). Neuropathology of Parkinson's disease. J. Neuropathol. Exp. Neurol. *55*, 259–272.

Giasson, B.I., Duda, J.E., Quinn, S.M., Zhang, B., Trojanowski, J.Q., and Lee, V.M. (2002). Neuronal alpha-synucleinopathy with severe movement disorder in mice expressing A53T human alpha-synuclein. Neuron *34*, 521–533.

Greggio, E., Jain, S., Kingsbury, A., Bandopadhyay, R., Lewis, P., Kaganovich, A., van der Brug, M.P., Beilina, A., Blackinton, J., Thomas, K.J., et al. (2006). Kinase activity is required for the toxic effects of mutant LRRK2/dardarin. Neurobiol. Dis. *23*, 329–341.

Hara, T., Nakamura, K., Matsui, M., Yamamoto, A., Nakahara, Y., Suzuki-Migishima, R., Yokoyama, M., Mishima, K., Saito, I., Okano, H., and Mizushima, N. (2006). Suppression of basal autophagy in neural cells causes neurodegenerative disease in mice. Nature *441*, 885–889.

Hinkle, K.M., Yue, M., Behrouz, B., Dächsel, J.C., Lincoln, S.J., Bowles, E.E., Beevers, J.E., Dugger, B., Winner, B., Prots, I., et al. (2012). LRRK2 knockout mice have an intact dopaminergic system but display alterations in exploratory and motor co-ordination behaviors. Mol. Neurodegener. *7*, 25.

Hulihan, M.M., Ishihara-Paul, L., Kachergus, J., Warren, L., Amouri, R., Elango, R., Prinjha, R.K., Upmanyu, R., Kefi, M., Zouari, M., et al. (2008). LRRK2 Gly2019Ser penetrance in Arab-Berber patients from Tunisia: A case-control genetic study. Lancet Neurol. *7*, 591–594.

Ichimura, Y., Kominami, E., Tanaka, K., and Komatsu, M. (2008). Selective turnover of p62/A170/SQSTM1 by autophagy. Autophagy *4*, 1063–1066.

Kabeya, Y., Mizushima, N., Ueno, T., Yamamoto, A., Kirisako, T., Noda, T., Kominami, E., Ohsumi, Y., and Yoshimori, T. (2000). LC3, a mammalian homologue of yeast Apg8p, is localized in autophagosome membranes after processing. EMBO J. *19*, 5720–5728.

Kachergus, J., Mata, I.F., Hulihan, M., Taylor, J.P., Lincoln, S., Aasly, J., Gibson, J.M., Ross, O.A., Lynch, T., Wiley, J., et al. (2005). Identification of a novel LRRK2 mutation linked to autosomal dominant parkinsonism: Evidence of a common founder across European populations. Am. J. Hum. Genet. *76*, 672–680.

Kirisako, T., Baba, M., Ishihara, N., Miyazawa, K., Ohsumi, M., Yoshimori, T., Noda, T., and Ohsumi, Y. (1999). Formation process of autophagosome is traced with Apg8/Aut7p in yeast. J. Cell Biol. *147*, 435–446.

Komatsu, M., Waguri, S., Chiba, T., Murata, S., Iwata, J., Tanida, I., Ueno, T., Koike, M., Uchiyama, Y., Kominami, E., and Tanaka, K. (2006). Loss of autophagy in the central nervous system causes neurodegeneration in mice. Nature *441*, 880–884.

Komatsu, M., Wang, Q.J., Holstein, G.R., Friedrich, V.L., Jr., Iwata, J., Kominami, E., Chait, B.T., Tanaka, K., and Yue, Z. (2007). Essential role for autophagy protein Atg7 in the maintenance of axonal homeostasis and the prevention of axonal degeneration. Proc. Natl. Acad. Sci. USA *104*, 14489–14494.

Kuwahara, T., Inoue, K., D'Agati, V.D., Fujimoto, T., Eguchi, T., Saha, S., Wolozin, B., Iwatsubo, T., and Abeliovich, A. (2016). LRRK2 and RAB7L1 coordinately regulate axonal morphology and lysosome integrity in diverse cellular contexts. Sci. Rep. *6*, 29945.

Lee, M.K., Stirling, W., Xu, Y., Xu, X., Qui, D., Mandir, A.S., Dawson, T.M., Copeland, N.G., Jenkins, N.A., and Price, D.L. (2002). Human alpha-synuclein-harboring familial Parkinson's disease-linked Ala-53–> Thr mutation causes neurodegenerative disease with alpha-synuclein aggregation in transgenic mice. Proc. Natl. Acad. Sci. USA *99*, 8968–8973.

Lesage, S., Leutenegger, A.L., Ibanez, P., Janin, S., Lohmann, E., Dürr, A., and Brice, A.; French Parkinson's Disease Genetics Study Group (2005). LRRK2 haplotype analyses in European and North African families with Parkinson disease: A common founder for the G2019S mutation dating from the 13th century. Am. J. Hum. Genet. *77*, 330–332.

Li, Y., Liu, W., Oo, T.F., Wang, L., Tang, Y., Jackson-Lewis, V., Zhou, C., Geghman, K., Bogdanov, M., Przedborski, S., et al. (2009). Mutant LRRK2 (R1441G) BAC transgenic mice recapitulate cardinal features of Parkinson's disease. Nat. Neurosci. *12*, 826–828.

Li, X., Patel, J.C., Wang, J., Avshalumov, M.V., Nicholson, C., Buxbaum, J.D., Elder, G.A., Rice, M.E., and Yue, Z. (2010). Enhanced striatal dopamine transmission and motor performance with LRRK2 overexpression in mice is eliminated by familial Parkinson's disease mutation G2019S. J. Neurosci. *30*, 1788–1797.

Lin, X., Parisiadou, L., Gu, X.L., Wang, L., Shim, H., Sun, L., Xie, C., Long, C.X., Yang, W.J., Ding, J., et al. (2009). Leucine-rich repeat kinase 2 regulates the progression of neuropathology induced by Parkinson's-disease-related mutant alpha-synuclein. Neuron *64*, 807–827.

Liu, G., Sgobio, C., Gu, X., Sun, L., Lin, X., Yu, J., Parisiadou, L., Xie, C., Sastry, N., Ding, J., et al. (2015). Selective expression of Parkinson's disease-related leucine-rich repeat kinase 2 G2019S missense mutation in midbrain dopaminergic neurons impairs dopamine release and dopaminergic gene expression. Hum. Mol. Genet. *24*, 5299–5312.

Marder, K., Wang, Y., Alcalay, R.N., Mejia-Santana, H., Tang, M.-X., Lee, A., Raymond, D., Mirelman, A., Saunders-Pullman, R., Clark, L., et al.; LRRK2 Ashkenazi Jewish Consortium (2015). Age-specific penetrance of LRRK2 G2019S in the Michael J. Fox Ashkenazi Jewish LRRK2 Consortium. Neurology *85*, 89–95.

Melrose, H.L., Dächsel, J.C., Behrouz, B., Lincoln, S.J., Yue, M., Hinkle, K.M., Kent, C.B., Korvatska, E., Taylor, J.P., Witten, L., et al. (2010). Impaired dopaminergic neurotransmission and microtubule-associated protein tau alterations in human LRRK2 transgenic mice. Neurobiol. Dis. *40*, 503–517.

Mizushima, N., Yoshimori, T., and Levine, B. (2010). Methods in mammalian autophagy research. Cell *140*, 313–326.

Nalls, M.A., Pankratz, N., Lill, C.M., Do, C.B., Hernandez, D.G., Saad, M., DeStefano, A.L., Kara, E., Bras, J., Sharma, M., et al.; International Parkinson's Disease Genomics Consortium (IPDGC); Parkinson's Study Group (PSG) Parkinson's Research: The Organized GENetics Initiative (PROGENI); 23andMe; GenePD; NeuroGenetics Research Consortium (NGRC); Hussman Institute of Human Genomics (HIHG); Ashkenazi Jewish

Dataset Investigator; Cohorts for Health and Aging Research in Genetic Epidemiology (CHARGE); North American Brain Expression Consortium (NABEC); United Kingdom Brain Expression Consortium (UKBEC); Greek Parkinson's Disease Consortium; Alzheimer Genetic Analysis Group (2014). Large-scale meta-analysis of genome-wide association data identifies six new risk loci for Parkinson's disease. Nat. Genet. *46*, 989–993.

Nichols, R.J., Dzamko, N., Morrice, N.A., Campbell, D.G., Deak, M., Ordureau, A., Macartney, T., Tong, Y., Shen, J., Prescott, A.R., and Alessi, D.R. (2010). 14-3-3 binding to LRRK2 is disrupted by multiple Parkinson's disease-associated mutations and regulates cytoplasmic localization. Biochem. J. *430*, 393–404.

Paisán-Ruíz, C., Jain, S., Evans, E.W., Gilks, W.P., Simón, J., van der Brug, M., López de Munain, A., Aparicio, S., Gil, A.M., Khan, N., et al. (2004). Cloning of the gene containing mutations that cause PARK8-linked Parkinson's disease. Neuron *44*, 595–600.

Pan, P.Y., and Yue, Z. (2014). Genetic causes of Parkinson's disease and their links to autophagy regulation. Parkinsonism Relat. Disord. *20* (*Suppl 1*), S154–S157.

Satake, W., Nakabayashi, Y., Mizuta, I., Hirota, Y., Ito, C., Kubo, M., Kawaguchi, T., Tsunoda, T., Watanabe, M., Takeda, A., et al. (2009). Genome-wide association study identifies common variants at four loci as genetic risk factors for Parkinson's disease. Nat. Genet. *41*, 1303–1307.

Shen, J. (2004). Protein kinases linked to the pathogenesis of Parkinson's disease. Neuron *44*, 575–577.

Sheng, Z., Zhang, S., Bustos, D., Kleinheinz, T., Le Pichon, C.E., Dominguez, S.L., Solanoy, H.O., Drummond, J., Zhang, X., Ding, X., et al. (2012). Autophosphorylation is an indicator of LRRK2 kinase activity and contributes to the cellular effects of PD mutations. Sci. Transl. Med. *4*, 164ra161.

Simón-Sánchez, J., Schulte, C., Bras, J.M., Sharma, M., Gibbs, J.R., Berg, D., Paisan-Ruiz, C., Lichtner, P., Scholz, S.W., Hernandez, D.G., et al. (2009). Genome-wide association study reveals genetic risk underlying Parkinson's disease. Nat. Genet. *41*, 1308–1312.

Skibinski, G., Nakamura, K., Cookson, M.R., and Finkbeiner, S. (2014). Mutant LRRK2 toxicity in neurons depends on LRRK2 levels and synuclein but not kinase activity or inclusion bodies. J. Neurosci. *34*, 418–433.

Spillantini, M.G., Schmidt, M.L., Lee, V.M., Trojanowski, J.Q., Jakes, R., and Goedert, M. (1997). Alpha-synuclein in Lewy bodies. Nature *388*, 839–840.

Steger, M., Tonelli, F., Ito, G., Davies, P., Trost, M., Vetter, M., Wachter, S., Lorentzen, E., Duddy, G., Wilson, S., et al. (2016). Phosphoproteomics reveals that Parkinson's disease kinase LRRK2 regulates a subset of Rab GTPases. eLife *5*, e12813.

Tong, Y., Yamaguchi, H., Giaime, E., Boyle, S., Kopan, R., Kelleher, R.J., 3rd, and Shen, J. (2010). Loss of leucine-rich repeat kinase 2 causes impairment of protein degradation pathways, accumulation of alpha-synuclein, and apoptotic cell death in aged mice. Proc. Natl. Acad. Sci. USA *107*, 9879–9884.

Tong, Y., Giaime, E., Yamaguchi, H., Ichimura, T., Liu, Y., Si, H., Cai, H., Bonventre, J.V., and Shen, J. (2012). Loss of leucine-rich repeat kinase 2 causes age-dependent bi-phasic alterations of the autophagy pathway. Mol. Neurodegener. *7*, 2.

Toyofuku, T., Morimoto, K., Sasawatari, S., and Kumanogoh, A. (2015). Leucine-rich repeat kinase 1 regulates autophagy through turning on TBC1D2-dependent Rab7 inactivation. Mol. Cell. Biol. *35*, 3044–3058.

Tsika, E., and Moore, D.J. (2012). Mechanisms of LRRK2-mediated neurodegeneration. Curr. Neurol. Neurosci. Rep. *12*, 251–260.

Tsika, E., Kannan, M., Foo, C.S., Dikeman, D., Glauser, L., Gellhaar, S., Galter, D., Knott, G.W., Dawson, T.M., Dawson, V.L., and Moore, D.J. (2014). Conditional expression of Parkinson's disease-related R1441C LRRK2 in midbrain dopaminergic neurons of mice causes nuclear abnormalities without neurodegeneration. Neurobiol. Dis. *71*, 345–358.

Tucci, A., Nalls, M.A., Houlden, H., Revesz, T., Singleton, A.B., Wood, N.W., Hardy, J., and Paisán-Ruiz, C. (2010). Genetic variability at the PARK16 locus. Eur. J. Hum. Genet. *18*, 1356–1359.

West, A.B., Moore, D.J., Biskup, S., Bugayenko, A., Smith, W.W., Ross, C.A., Dawson, V.L., and Dawson, T.M. (2005). Parkinson's disease-associated mutations in leucine-rich repeat kinase 2 augment kinase activity. Proc. Natl. Acad. Sci. USA *102*, 16842–16847.

Westerlund, M., Belin, A.C., Anvret, A., Bickford, P., Olson, L., and Galter, D. (2008). Developmental regulation of leucine-rich repeat kinase 1 and 2 expression in the brain and other rodent and human organs: Implications for Parkinson's disease. Neuroscience *152*, 429–436.

Yamaguchi, H., and Shen, J. (2013). Histological analysis of neurodegeneration in the mouse brain. Methods Mol. Biol. *1004*, 91–113.

Yu, H., Saura, C.A., Choi, S.Y., Sun, L.D., Yang, X., Handler, M., Kawarabayashi, T., Younkin, L., Fedeles, B., Wilson, M.A., et al. (2001). APP processing and synaptic plasticity in presenilin-1 conditional knockout mice. Neuron *31*, 713–726.

Zimprich, A., Biskup, S., Leitner, P., Lichtner, P., Farrer, M., Lincoln, S., Kachergus, J., Hulihan, M., Uitti, R.J., Calne, D.B., et al. (2004). Mutations in LRRK2 cause autosomal-dominant parkinsonism with pleomorphic pathology. Neuron *44*, 601–607.

STAR★METHODS

KEY RESOURCES TABLE

REAGENT or RESOURCE	SOURCE	IDENTIFIER
Antibodies		
Rabbit anti-LRRK1	Thermo Fisher Scientific	Cat # PA5-13868 RRID: AB_2297136
Rabbit anti-LRRK2	Tong et al., 2010 Shen lab	N/A
Mouse anti-spectrin	Sigma-Aldrich	Cat # S3396 RRID: AB_261487
Rabbit anti-α-synuclein	Santa Cruz	Cat # sc-7011-R RRID: AB_2192953
Rabbit anti-ubiquitin	Abcam	Cat # ab7780 RRID: AB_306069
Guinea pig anti-p62	Progen	Cat # GP62-C RRID: AB_2687531
Rabbit anti-LC3	Sigma-Aldrich	Cat # L7543 RRID: AB_796155
Mouse anti-β-actin	Cell signaling	Cat # 3700S RRID: AB_2242334
Mouse anti-β-tubulin	Sigma-Aldrich	Cat # T8660 RRID: AB_477590
Anti-Tyrosine Hydroxylase antibody	Abcam	Cat # AB49640 RRID: AB_883323
Rabbit anti-cleaved caspases-3	Cell Signaling	Cat # 9661S RRID: AB_2341188
Mouse anti-NeuN	Milipore Sigma	Cat # MAB377 RRID: AB_2298772
Mouse anti-DARPP-32	Thermo Fisher Scientific	Cat # MA5-14968 RRID: AB_10981784
Mouse anti-calbindin-D-28K	Sigma-Aldrich	Cat # C9848 RRID: AB_476894
Goat anti-Rabbit IRdye680 Secondary Antibody	LI-COR Bioscience	Cat # 926-68071 RRID: AB_10956166
Goat anti-mouse IRdye680 Secondary Antibody	LI-COR Bioscience	Cat # 925-68070 RRID: AB_2651128
Donkey anti-guinea pig IRdye680 Secondary Antibody	LI-COR Bioscience	Cat # 926-68077 RRID: AB_10956079
Goat anti-Rabbit IRdye800 Secondary Antibody	LI-COR Bioscience	Cat # 925-32211 RRID: AB_2651127
Goat anti-mouse IRdye800 Secondary Antibody	LI-COR Bioscience	Cat # 925-32210 RRID: AB_2687825
Goat anti-Rat IRdye800 Secondary Antibody	LI-COR Bioscience	Cat # 925-32219 RRID: AB_1850025
Donkey anti-guinea pig IRdye800 Secondary Antibody	LI-COR Bioscience	Cat # 926-32411 RRID: AB_1850024
Alexa Fluor® 555 Goat Anti-Rabbit IgG (H+L)	Thermo Fisher Scientific	Cat # A21429 RRID: AB_141761
Alexa Fluor® 647 Goat Anti-Mouse IgG (H+L)	Thermo Fisher Scientific	Cat # A21236 RRID: AB_2535805
Goat anti-Rabbit Alexa Fluor 488-conjugated secondary antibodies	Thermo Fisher Scientific	Cat # A-21311 RRID: AB_221477
Chemicals, Peptides, and Recombinant Proteins		
TRIzol®	Sigma-Aldrich	Cat # T9424
MicroPoly(A)Purist kit	Thermo Fisher Scientific	Cat # AM1922
Vectastain Elite ABC reagent	Vector laboratories	Cat # PK-6100
Superscript II	Thermo Fisher Scientific	Cat # 18064
RIPA buffer	Thermo Fisher Scientific	Cat # 89900
Propyleneoxide and TAAB Epon	Marivac Canada Inc	N/A
Protease Inhibitor Cocktail	Sigma-Aldrich	Cat # P8340
Phosphatase Inhibitor Cocktail	Sigma-Aldrich	Cat # P2850
Procaine hydrochlorid	Sigma-Aldrich	Cat # P9879
Methanol (For HPLC)	Sigma-Aldrich	Cat # 34860
Heparin	Sigma-Aldrich	Cat # H4784
Normal Goat Serum Blocking Solution	Vector laboratories	Cat # S-1000
Formaldehyde/Glutaraldehyde	Electron Microscopy Science	Cat # 15949
Nitrocellulose Membrane	Thermo Fisher Scientific	Cat # 88018
Biotinylated Rabbit Anti-Sheep IgG Antibody	Vector laboratories	Cat # BA-6000
DAB Peroxidase Substrate Kit	Vector laboratories	Cat # SK-4100

(*Continued on next page*)

Continued		
REAGENT or RESOURCE	SOURCE	IDENTIFIER
Biotinylated Goat Anti-Rabbit IgG Antibody	Vector laboratories	Cat # BA-1000
Biotinylated Goat Anti-Mouse IgG Antibody	Vector laboratories	Cat # BA-9200
VECTASHIELD Mounting Medium	Vector laboratories	Cat # H-1000
Mouse Synuclein Alpha ELISA Kit	Neo Scientific	Cat # MS0040
Experimental Models: Cell Lines		
LRRK1 "knockout-first" ES cell clone	KOMP Repository	EPD0073_6_C01
Experimental Models: Organisms/Strains		
Mouse: B6129SF1/J	The Jackson Laboratory	Jax No: 101043
Mouse: *αCaMKII-Cre* transgenic	Yu et al., 2001	N/A
Mouse: *LRRK2*$^{-/-}$ (B6;129-*Lrrk2*$^{tm2.1Shn}$/J)	Tong et al., 2010; The Jackson Laboratory	Jax No: 016209
Mouse: *LRRK1*$^{-/-}$ (Line1)	This paper	N/A
Mouse: *LRRK1*$^{-/-}$ (Line2)	This paper	N/A
Mouse: *LRRK*$^{-/-}$ (DKO)	This paper	N/A
Oligonucleotides		
LRRK1 PCR Forward Primer for 5′ Southern Probe (Intron 2): 5′-GACTTCCGAAGCCTGTTTGTCAG-3′	This paper	N/A
LRRK1 PCR Reverse Primer for 5′ Southern Probe (Exon 3/Intron 3): 5′-CTACCTTCTCCTGTGAGGATTCGCT-3′	This paper	N/A
LRRK1 PCR Forward Primer for 3′ Southern Probe (Intron 6): 5′-GGTCATGATGGTCTATCACAGCAATAGT-3′	This paper	N/A
LRRK1 PCR Reverse Primer for 3′ Southern Probe (Intron 6): 5′-GATGCACTCACAGTCTTCGTGACTC-3′	This paper	N/A
LRRK1 PCR Forward Primer for Exons 25-31 cDNA Northern Probe: 5′-GCAGTGGCACAGTCATCTACCA-3′	This paper	N/A
LRRK1 PCR Reverse Primer for Exons 25-31 cDNA Northern Probe: 5′-GGCACATACCCTTAAGGCTGTAGA-3′	This paper	N/A
LRRK1 PCR Forward Primer for Exons 2-3 cDNA Northern Probe: 5′-CAGGATGAGCGTGTGTCTGCAG-3′	This paper	N/A
LRRK1 PCR Reverse Primer for Exons 2-3 cDNA Northern Probe: 5′-CCTTCTCCTGTGAGGATTCGCTCT-3′	This paper	N/A
LRRK1 Forward Primer for RT-PCR (Exon 3): 5′-CGAAGACATGGGCAGCAAACTG-3′	This paper	N/A
LRRK1 Reverse Primer for RT-PCR (Exon 6): 5′-GCTCAGGACTATCCAGCAGGATGTAG-3′	This paper	N/A
Software and Algorithms		
Image-Studio	Odyssey	5.2
PRISM 7	GraphPad	7.0
ImageJ software	NIH	1.50i
CellSens Entry	Olympus	1.5
Bioquant Life Science	Bioquant Life Science	13.5.6

CONTACT FOR REAGENT AND RESOURCE SHARING

Further information and requests for resources and reagents should be directed to and will be fulfilled by the Lead Contact, Dr. Jie Shen (jshen@bwh.harvard.edu).

EXPERIMENTAL MODEL AND SUBJECT DETAILS

Mouse Strains and Animal Care

All mice were housed in humidity- and temperature-controlled rooms maintained on a 12:12h light: dark cycle and were given standard rodent chow and water. Three genetic *LRRK* mutant mouse lines were used in the current study: *LRRK2*$^{-/-}$ (*LRRK2* KO1) mice were described previously (Tong et al., 2010), *LRRK1*$^{-/-}$ and *LRRK* DKO mice were generated in this study. All three mutant genotypes and wild-type control mice were maintained on a C57BL/6J and 129 hybrid genetic background. *LRRK* DKO and littermate wild-type mice were obtained from breeding *LRRK1*$^{+/-}$; *LRRK2*$^{+/-}$ mice together. Most of the data from mice at 2, 8 and 15 months of age were obtained from analysis of *LRRK* DKO and wild-type mice, which were either littermates or from the same breeding pairs. Because of the low ratio (1/16) to obtain *LRRK* DKO and littermate wild-type mice, we subsequently used breeding pairs of *LRRK* DKO (or wild-type) mice crossing with each other to obtain more *LRRK* DKO (or wild-type mice). In this instance, the *LRRK* DKO and wild-type mice used in breeding were littermates or different litters from the same parents, so the resulting *LRRK* DKO and wild-type mice were only one generation apart in terms of their genetic background.

All procedures were approved by the IACUC committees of Harvard Medical School and Brigham and Women's Hospital, and conform to the USDA Animal Welfare Act, PHS Policy on Humane Care and Use of Laboratory Animals, the "ILAR Guide for the Care and Use of Laboratory Animals" and other applicable laws and regulations.

METHOD DETAILS

Generation of *LRRK1*$^{-/-}$ and *LRRK*$^{-/-}$ mice

To generate *LRRK1*$^{-/-}$ mice, we purchased the ES cell clone carrying the *LRRK1* "knockout-first" allele (EPD0073_6_C01) from the KOMP Repository (https://www.komp.org/) funded by the trans-NIH Knock-Out Mouse Project. The targeting vector contains a 5′ homologous arm (4.6 kb of *LRRK1* introns 3), the gene-trapping and selection cassettes and a 3′ homologous arm (6.8 kb encompassing exons 4, 5, and 6). The entire *En2SA-IRES-lacZ* and *hbactP-neo* sequence is flanked by two *FRT* sites, and the *hbactP-neo* cassette is flanked by two *loxP* sites. The *En2SA-IRES-lacZ* trapping cassette includes the mouse En2 splice acceptor (En2SA), which contains intron 2 and exon 2 of the *engrailed* gene, the *internal ribosome entry site* (*IRES*) sequence, and the *lacZ* gene. The floxed *neo* cassette contains the human β-actin promoter, the *neo* cDNA and the SV40 polyadenylation sequence. A third *loxP* site was introduced into *LRRK1* intron 5, allowing for removal of exons 4-5 in the presence of Cre recombinase. The targeting vector was introduced into ES cells derived from B6 mice.

We expanded the ES cells and verified the correct homologous recombination events by Southern blotting. Genomic ES DNA was digested with EcoRV or NheI, and the 5′ and 3′ external probes were used to confirm proper recombination in the 5′ and 3′ homologous regions, respectively. The PCR primer sequences for the 5′ external probe (584 bp) are 5′-GACTTCCGAAGC CTGTTTGTCAG-3′ and 5′-CTACCTTCTCCTGTGAGGATTCGCT-3′, and the primer sequences for the 3′ external probe (867 bp) are 5′-GGTCATGATGGTCTATCACAGCAATAGT-3′ and 5′-GATGCACTCACAGTCTTCGTGACTC-3′. We also confirmed that there is no random insertion of the targeting vector in the genome by Southern analysis using a *neo* cDNA probe. ES cells from the confirmed clone were injected into BALB/c blastocysts to generate chimeric mice. Mice carrying the targeted allele were bred to B6/129 F1 mice to generate heterozygous *LRRK1* mice. The germline transmission of the targeted *LRRK1* allele was confirmed using PCR and Southern blotting.

LRRK1 targeted mice (Line 1) were bred with *αCaMKII-Cre* transgenic mice to remove the floxed *neo* cassette and *LRRK1* exons 4-5, because *αCaMKII* is expressed in male gametes (Ackermann et al., 2009). The resulting heterozygous mice (Line 2) were confirmed by Southern blotting for correct Cre-mediated recombination and proper removal of the *neo* cassette and *LRRK1* exons 4-5, and by Northern and Western analyses for the absence of *LRRK1* mRNA and protein. To generate *LRRK* DKO mice, *LRRK1*$^{-/-}$ mice were crossed with our homozygous *LRRK2* KO1 mice described previously (Tong et al., 2010) to obtain *LRRK1*$^{+/-}$; *LRRK2*$^{+/-}$ mice, which were further intercrossed to generate *LRRK* DKO mice and controls for further phenotypic analysis.

Northern analysis

Total RNA was isolated from brains or kidneys using TRIzol® (Sigma), and polyA+ RNA were enriched using the MicroPoly(A)Purist kit (Ambion). Probes were synthesized using Prime-It II random labeling kit (Stratagene) and then used for membrane hybridization at 50°C overnight. The PCR primer sequences used to amplify cDNA probes are as follows: 5′-GCAGTGGCACAGTCATCTACCA-3′ and 5′-GGCACATACCCTTAAGGCTGTAGA-3′ for the probe specific for *LRRK1* exons 25-31, 5′-CAGGATGAGCGTGTGTCTGCAG-3′ and 5′- CCTTCTCCTGTGAGGATTCGCTCT-3′ for the probe specific for *LRRK1* exons 2-3. NIH ImageJ software was used to quantify the level of transcripts by comparing the intensities of the bands after subtracting the background.

RT-PCR

To perform real-time quantitative RT-PCR, total RNA isolated from brains and kidneys was used to synthesize cDNA (Superscript II from Invitrogen). Real-time PCR was performed in triplicate on a 96 well plate using an ABI 7900 detection system to assess the relative level of murine *LRRK1* mRNA using a probe spans exons 30 and 31 (Mm00713303_m1, Applied Biosystems). Murine TBP (Mm00446973_m1) was used as the endogenous reference gene. Data plotted as mean ± SEM. For non-quantitative RT-PCR,

the sequences of the primers used in RT and PCR are as follows 5′-CGAAGACATGGGCAGCAAACTG-3′ for *LRRK1* exon 3 and 5′-GGCTCAGGACTATCCAGCAGGATGTAG-3′ for *LRRK1* exon 6. The identity of the PCR product was confirmed by sequencing.

Western analysis

The striatum, neocortex, and optical nerve were dissected from the brain, and they were harvested from *LRRK* DKO mice and controls. Fresh tissues were homogenized in an ice-cold stringent RIPA buffer (50 mM Tris-HCl, pH 7.4, 150 mM NaCl, 0.1% SDS, 1% Triton X-100, 1% sodium deoxycholate, supplemented with protease inhibitor mixture and phosphatase inhibitor mixtures; from Sigma), followed by sonication. Homogenates were centrifuged at 14,000 × g for 20 min at 4°C to separate supernatants (RIPA buffer-soluble fractions). Equal amounts of total proteins from each preparation were loaded and separated on NuPAGE gels (Invitrogen) and transferred to nitrocellulose membranes. After blocking membranes were incubated at 4°C overnight with primary antibodies. Primary antibodies used were rabbit anti-LRRK1 (1:250; Thermo scientific), rabbit anti-LRRK2 (1:1000; made in-house), mouse anti-spectrin (1:10000; Sigma), rabbit anti-α-synuclein (1:1000; Santa Cruz), rabbit anti-ubiquitin (1:1000; Abcam), guinea pig anti-p62 (1:1000; Progen), rabbit anti-LC3 (1:1000; Sigma), mouse anti-β-actin (1:10000; Cell Signaling), and mouse anti-β-tublin (1:1000; Sigma). Membranes were then incubated with dye-coupled secondary antibodies (goat anti-rabbit IRdye680, goat anti-mouse IRdye680, donkey anti-guinea pig IRdye680, goat anti-rabbit IRdye800, goat anti-rat IRdye800, goat anti-mouse IRdye800 and donkey anti-guinea pig IRdye800 from LI-COR Bioscience). Signals were quantified using the Odyssey Infrared Imaging System (LI-COR Bioscience).

Histological analysis

Mice were anesthetized and then transcardially perfused with Ringer's solution containing 0.25 g/L heparin (Sigma) and 5 g/L procaine (Sigma) followed by ice-cold 4% formaldehyde in phosphate buffered saline (pH 7.4) (Electron Microscopy Sciences). Brains were post-fixed in 4% formaldehyde at 4°C overnight and then processed for paraffin embedding following standard procedures. Coronal brain sections were cut at 16 μm thickness, and sagittal sections were cut at 10 μm.

Immunohistochemical analysis

Coronal sections containing the SNpc or LC or neocortex and striatum and optic tract were selected, deparaffinized, rehydrated. All brain sections, except those for TH immunostaining, were subjected to permeabilization with a solution containing 0.1% Triton X-100, 0.1% sodium citrate in PBS and antigen retrieval by microwaving for 10 min in 10 mM sodium citrate buffer, pH 6.0. Endogenous peroxidase activity was quenched by incubating in 0.3% H_2O_2 in methanol. Sections were then blocked with a solution containing 5% normal goat serum for 1 hr at room temperature (Vector Laboratories). After blocking, sections were incubated with primary antibodies overnight at 4°C. Primary antibodies were rabbit anti-TH (1:1000; Chemicon), rabbit anti-cleaved caspases-3 (1:150, Cell Signaling Technology), rabbit anti-α-synuclein (1:500; Santa Cruz), rabbit anti-ubiquitin (1:250; Abcam), or guinea-pig anti-p62 (1:200, Progen), followed by 1 hr incubation with biotinylated secondary antibodies and 1 hr incubation with Vectastain Elite ABC reagent and then developed using chromogenic DAB substrate (Vector Laboratories) as previously described (Yamaguchi and Shen, 2013). For negative controls, primary antibodies alone or together with secondary antibodies were omitted from the incubation buffer. The number of apoptotic cells labeled by active caspase-3 antibodies was quantified using 3-6 coronal sections (5-10 sections apart), and the average number of apoptotic cells in the SNpc, striatum or neocortex per brain section was shown in the figure. The immunoreactivity of α-synuclein, ubiquitin or p62 was quantified using 2-6 coronal sections (10 sections apart), and the average immunoreactivity in the SNpc, striatum or neocortex per brain section was shown in the figure.

For NeuN and TH double immunostaining, coronal sections were deparaffinized, rehydrated, followed by quenching of the endogenous peroxidase activity using 0.3% H_2O_2 in methanol. Sections were then blocked with a solution containing 5% normal goat serum for 1 hr at room temperature. After blocking, sections were incubated with mouse anti-NeuN (1:300; Milipore) antibody overnight at 4°C, followed by 1 hr incubation with biotinylated mouse secondary antibodies and 1 hr incubation with Vectastain Elite ABC reagent and then developed using chromogenic DAB substrate (brown color). Following several washes using 1x PBS, sections were then incubated with rabbit anti-TH antibody (1:1000; Chemicon) overnight at 4°C, followed by 1 hr incubation with biotinylated rabbit secondary antibodies and 1 hr incubation with Vectastain Elite ABC reagent and then developed using chromogenic DAB substrate containing Nickel (gray color) (Vector Laboratories).

Stereological neuron count

For stereological neuron count of DA and noradrenergic neurons, coronal sections were immunostained with TH antibody (1:1000; Chemicon). For *LRRK* DKO, *LRRK1* KO, *LRRK2* KO and wild-type mice at the ages of 12, 14 and 15 months, every 5th coronal sections were used, whereas every 10th coronal sections were used for mice at 2, 8 and 10 months. The number of DA neurons in the SNpc or noradrenergic neurons in the LC was determined using the fractionator and optical dissector method and was calculated to reflect both hemispheres. For the neocortex, every 40th sagittal sections were stained with 0.5% cresyl violet (Nissl) or immunostained with mouse anti-NeuN (1:300; Milipore) antibodies. The cortical volume (Nissl) was quantified and was calculated to reflect both hemispheres, and the number of cortical neurons (NeuN+) was quantified. For the striatum, every 40th sagittal sections were immunostained with mouse anti-DARPP-32 (1:200; Thermo scientific) antibodies, and the number of DARPP-32+ cells and the volume of the striatum were quantified. For the cerebellum, every 10th sagittal sections were immunostained with the mouse

anti-calbindin-D-28K (1:500; Sigma) antibody, and the cerebellar volume and the Purkinje cell number were quantified. The stereological neuron or volume quantification was done using the fractionator and optical dissector methods under an Olympus BX51 light microscope equipped with a CCD camera connected to a computer running Bioquant image analysis software. Images were captured using Olympus BX40 Dual Viewing Microscope.

TUNEL

Brain sections containing the SNpc or neocortex (coronal, 7 sections apart) or the striatum (sagittal, 40 sections apart) were chosen for the analysis. Deparaffinized and rehydrated brain sections were subjected to permeabilization with a solution containing 0.1% Triton X-100, 0.1% sodium citrate in PBS for 8 min and then immersed in 10 mM citrate buffer (pH 6.0) and boiled in a microwave oven for antigen retrieval for 5 min. For TUNEL, slides were blocked in 5% of goat serum for 60 min followed by treatment with fluorescein (Roche) at 37°C for 1 hr. The slides were then washed in PBS three times. For TUNEL and TH or DARPP-32 or NeuN co-labeling, sections were incubated with primary antibodies overnight at 4°C; primary antibodies were TH, DARPP-32 (1:200; Thermo scientific) or NeuN, followed by 1 hr incubation with appropriate Alexa Fluor 488-conjugated secondary antibodies (Molecular Probes). Images were captured sequentially for TUNEL fluorescence (excitation: 559 nm, emission range: 575–675 nm) and TH, DARPP-32 or NeuN (excitation: 473 nm, emission range: 490–540 nm) using an Olympus FluoView FV1000 confocal microscope. The quantification of the fluorescence was analyzed using the ImageJ software. The number of apoptotic cells labeled by TUNEL was quantified using 2 sections, and the average number of apoptotic cells in the SNpc, striatum or neocortex per brain section was shown in the figure.

Measurements of striatal DA and its metabolites by HPLC

The striatum was dissected, weighed, and stored at −80°C until use. Frozen striata were sonicated in ice-cold solution (0.1 M perchloric acid/0.2 mM sodium bisulfite) and centrifuged for 10 min at 14,000 × g at 4°C. The supernatant was filtered and applied to C18 reverse phase HPLC columns connected to an Alexys LC-100 system (Antec-Leyden, Hanover, MD, USA) with electrochemical detection (DECADE II) and a VT-03 electrochemical flow cell. DA measurements were made using a detection potential of 320 mV and isocratic elution (50 mM phosphoric acid, 500 mg/L octane sulfonic acid, 0.1 mM EDTA, 8 mM KCl, pH 6.0, and 10% methanol; from Sigma) through a 50 × 2.1 mm HPLC column at the flow rate of 0.2 mL/min. DA metabolites 3,4-dihydroxyphenylacetic acid (DOPAC) eluted isocratically on a 150 × 2.1 mm HPLC column at lower pH (50 mM phosphoric acid, 50 mM citric acid, 400 mg/L octane sulphonic acid, 0.1 mM EDTA, 8 mM KCl, pH 3.75, and 3% methanol) at the flow rate 0.2 mL/min and detected at 590 mV. Concentrations of DA, its metabolites, and DOPA in the striatal samples were obtained by comparing with a series of catecholamine standards of known concentrations, which were run under the same conditions. The levels of DA, its metabolites, and DOPA were normalized to tissue weight.

ELISA

Alpha-synuclein levels in the striatum and neocortex were assessed using Mouse synuclein, AlphaELISA Kit (Neo scientific) according to the manufacturer's protocol. Briefly, homogenates from the dissected striatum or neocortex were plated in duplicates and incubated in the presence of balance solution and enzyme solution in pre-blocked wells for 1 hr at 37°C. Substrates were added to each well and incubate at room temperature for 15 min after stop solution was added the optical density at 450 nm was measured.

Quantitative EM analysis

Mice were perfused with a fixative solution containing a mixture of 2.5% paraformaldehyde and 2.5% glutaraldehyde in 0.1 M sodium cacodylate buffer (pH 7.4) (Electron Microscopy Sciences, #1549, Hatfield, PA, USA). Brains were dissected and then placed on a vibratome to trim off the cerebellum and the anterior portion of the brain, and three coronal sections in 300 μm thickness spanning the SNpc region were post fixed overnight with the fixative solution at 4°C. One of the sections (300 μm) was used for TH immunostaining to confirm the presence of TH+ DA neurons in the SNpc. The adjacent section was used for EM analysis and left in the fixative until processing for embedding in resin. Embedding and ultrathin sectioning was done by the Harvard Medical School EM facility. In brief, the tissue was post fixed with 1% Osmium tetroxide (OsO4)/1.5% Potassium ferrocyanide (KFeCN6) for 1 hr, washed 2 times in water followed by 50mM Maleate buffer pH 5.15 (MB) and incubated in 1% uranyl acetate in MB for 1hr and dehydrated in ascending alcohols followed by incubation in propylene oxide. Tissue was incubated overnight in a 1:1 mixture of propylene oxide and TAAB Epon (Marivac Canada). The following day the samples were embedded in TAAB Epon and polymerized at 60°C for 48 hr. Ultrathin sections (about 80 nm) were cut on a Reichert Ultracut-S microtome, picked up on to copper grids stained with lead citrate and examined in a JEOL 1200EX Transmission electron microscope. Images were recorded with an AMT 2k CCD camera. For each brain area (Striatum and SNpc) a minimum of 10 micrographs containing an entire neuronal cell body were taken for each genotype and age, respectively.

A minimum of 10 micrographs containing the entire neuronal cell body was analyzed for each brain. The number of electron-dense autophagic and lysosomal vacuoles larger than 0.5 μm in diameter in each neuronal body was counted at a magnification of 2500-4000x. Higher magnification micrographs (10000-20000x) were taken to confirm the presence of autophagosomes and autolysosomes.

QUANTIFICATION AND STATISTICAL ANALYSIS

Data acquisition and quantification was performed in a genotype blind manner with the exception of the molecular analysis (Southern, Northern, Western). All statistical analyses were performed using Prism 7 (GraphPad Software) or Excel (Microsoft). All data are presented as the means ± SEM. The exact sample size (e.g., the number of mice, brains or neurons) of each experiment is provided in the relevant figures.

Statistical analyses were conducted using t tests (Figures 2B, 2D–2F, 3B, 3D, 3F, 4B, 4D, 4F, 4G, 5D, 5E, 6D, and 6F), one-way ANOVA followed up by Tukey's multiple comparisons tests (Figures 1E, 5B, 6B, and 7K) or one-way ANOVA followed up by Newman-Keuls multiple comparison tests (Figures 1F). All statistical comparisons were performed on data from $\geq$ 3 biologically independent samples and replicated on different experimental days. Significance is shown as *$p < 0.05$, **$p < 0.01$, ***$p < 0.001$, ****$p < 0.0001$, and not significant values are not noted.